The Extra-Islet Pancreas Supports Autoimmunity in Human Type 1 Diabetes

Barlow, G.L.[1,2,†], Schürch, C.M[2,4], Bhate, S.S.[2], Phillips, D.[2], Young, A.[3,6,7], Dong, S.[3,5] Martinez, HA.[1], Kaber, G.[1], Nagy, N. [1], Ramachandran S.[1], Meng, J.[1], Korpos E.[9] Bluestone, J.A.[†,8], Nolan, G.P.[†,2], Bollyky, P.L.[†,‡,1]

† Corresponding Author
‡ Lead Contact

Affiliations:

1. Division of Infectious Diseases and Geographic Medicine, Department of Medicine, Stanford University School of Medicine, Stanford, CA 94305, USA
2. Department of Pathology, Stanford University School of Medicine, Stanford, CA 94305, USA
3. Diabetes Center, University of California San Francisco, San Francisco, CA 94143, USA
4. Department of Pathology and Neuropathology, University Hospital and Comprehensive Cancer Center, Tübingen, Germany
5. Sean N. Parker Autoimmune Research Laboratory and Diabetes Center, University of California San Francisco, San Francisco, CA, USA
6. Huntsman Cancer Institute, University of Utah Health Sciences Center, Salt Lake City, UT 84112, USA
7. Department of Pathology, University of Utah School of Medicine, Salt Lake City, UT 84112, USA
8. Sonoma Biotherapeutics, South San Francisco, CA 94080 USA
9. Institute of Physiological Chemistry and Pathobiochemistry and Cells-in-Motion Interfaculty Center, University of Muenster, Germany

Further information and requests for resources and reagents should be directed to and will be fulfilled by the lead contact, Paul Bollyky (pbollyky@stanford.edu).

Abstract

In autoimmune Type 1 diabetes (T1D), immune cells infiltrate and destroy the islets of Langerhans – islands of endocrine tissue dispersed throughout the pancreas. However, the contribution of cellular programs outside islets to insulitis is unclear. Here, using CO-Detection by indEXing (CODEX) tissue imaging and cadaveric pancreas samples, we simultaneously examine islet and extra-islet inflammation in human T1D. We identify four sub-states of inflamed islets characterized by the activation profiles of $CD8^+$T cells enriched in islets relative to the surrounding tissue. We further find that the extra-islet space of lobules with extensive islet-infiltration differs from the extra-islet space of less infiltrated areas within the same tissue section. Finally, we identify lymphoid structures away from islets enriched in $CD45RA^+$ T cells – a population also enriched in one of the inflamed islet sub-states. Together, these data help define the coordination between islets and the extra-islet pancreas in the pathogenesis of human T1D.

Keywords: Type 1 Diabetes; Insulitis; Autoimmunity; Multiplexed Imaging; CODEX; Systems Immunology; Tissue Architecture

Main

In Type 1 diabetes (T1D), insulin-producing β-cells are killed by islet-infiltrating immune cells in a process called "insulitis". T1D results in a critical requirement for exogenous insulin and affects over eight million individuals world-wide with an estimated 0.5 million new diagnoses each year (Gregory et al. 2022).

Recently, the first immunotherapy for delaying T1D onset, teplizumab (a human anti-CD3 monoclonal antibody) was approved by the US Food and Drug Administration (Hirsch 2023). However, this treatment and other immunotherapies help only a small fraction of patients and are significantly less effective after patients progress to overt T1D (Herold et al. 2013; Perdigoto et al. 2019; Herold et al. 2019; Pescovitz et al. 2009; Orban et al. 2011; 2014; Bluestone, Buckner, and Herold 2021). A better understanding of T1D pathogenesis is essential to building on this progress.

One of the challenges of studying human T1D pathology is the availability of suitable tissue samples. Obtaining pancreatic biopsies raises the risk of surgical complications and the progressive nature of T1D would necessitate serial, longitudinal studies over time, which is prohibitive (Krogvold et al. 2014). Fortunately, the Juvenile Diabetes Research Foundation (JDRF) Network for Pancreatic Organ Donors with Diabetes (nPOD) have provided human pancreatic tissues from cadaveric donors for this study (Campbell-Thompson et al. 2012; Pugliese et al. 2014). nPOD has enabled substantial progress towards characterizing the pathology of human T1D (Wilcox et al. 2016; Arif et al. 2014; Leete et al. 2016; Martino et al. 2015; Korpos et al. 2021).

Our understanding of key features of human T1D pathology remains limited. Although the cellular composition of insulitis, inflammation specifically of the islets, has been studied extensively, this has been done in separate studies looking at different tissue sections, prohibiting an understanding of how the numerous cellular programs in insulitis are coordinated throughout disease. This was recently addressed using Imaging Mass Cytometry (IMC), which uncovered alterations in β-cell phenotypes, immune composition, vascular density, and basement membrane (Damond et al. 2019; Wang et al. 2019). However, these studies did not deeply phenotype islet-infiltrating $CD8^+$T cells, believed to be major driver of β-cell elimination.

Recently, intriguing differences in the extra-islet spaces of T1D and healthy controls have been reported. First, the abundance of multiple types of immune cells outside islets are increased in T1D patients compared to non-T1D controls (Rodriguez-Calvo et al. 2014; Campbell-Thompson, Rodriguez-Calvo, and Battaglia 2015; Bender et al. 2020). Second, HLA-DR expression is increased on ductal cells in T1D tissue donors, hinting at a functional link with $CD4^+$T cells (Fasolino et al. 2022). Third, peri-insulitis, the accumulation of immune cells outside islets, is observed in tissues from patients with T1D (Korpos et al. 2013), indicating that not all T cells enter the pancreas directly via islet microvasculature (Savinov et al. 2003). Fourth, in human T1D, but less so in most animal models, islets in different regions of the pancreas are infiltrated at strikingly different rates for reasons that are unknown (In't Veld 2014). This suggests that the extra-islet compartment could be responsible by governing the targeting of islets. Finally, tertiary lymphoid structures (TLS) – dense aggregates of lymphoid cells indicative of local immune activation – are observed outside islets in T1D patients (Korpos et al. 2021).

In summary, analyzing both compartments simultaneously could help identify how these extra-islet factors influence islet pathogenesis. However, to date, multiplexed imaging studies have only examined islets. A comprehensive, spatially resolved cellular analysis of both compartments in T1D is lacking.

Here, we investigated the islet and extra-islet pancreas together. We used CO-Detection by indexing (CODEX) with an antibody panel targeting 54 antigens to samples from a cohort of T1D patients with insulitis as well as non-T1D individuals with and without islet-specific autoantibodies (AA- and AA+ respectively) obtained through the JDRF nPOD program. We analyzed approximately 2000 islets and broad swaths of the extra-islet tissue to evaluate local and distal spatial architecture. We then used pseudotime analysis to characterize insulitis sub-states based on the activation states of islet-infiltrating $CD8^{+}$T cells. We further investigated the cellular changes in niches and lobules beyond islets. Our results implicate both the islet microenvironment and inflammation at distal sites within the pancreas in the progression of insulitis.

Cohort curation, image acquisition, and cell annotation

The JDRF nPOD is a national registry of cadaveric pancreases donated by T1D patients that has transformed the ability of researchers to investigate the pathways underlying the progression of human T1D (Campbell-Thompson et al. 2012; Pugliese et al. 2014). Insulitis is present in only a small fraction of T1D cases, including nPOD's (In't Veld 2011; Atkinson and Mirmira 2023). Although nPOD has close to 200 T1D cases, at the time of our study, nPOD had only 17 with documented insulitis. For some of these 17, tissues had been heavily sectioned and the current tissue blocks did not still contain insulitis. AA+ and T1D cases were selected by performing triple-immunohistochemistry for Insulin, Glucagon, and CD3. T1D and AA+ cases that had CD3+ staining in islet or peri-islet spaces and tissue still available were selected for our study. The final cohort included two AA+ cases, eight T1D cases, and three non-T1D controls. Given that insulitis is not detected in non-T1D cases (Bruggeman et al. 2021), the blocks from controls were selected randomly. The T1D cases varied in the time between diagnosis and death from 0 years (diagnosed at death) to 6 years (Figure 1.A**,** left). The causes of death were mostly unrelated to T1D complications (Supplemental Table 1). Therefore, the time since diagnosis is not a reflection of the severity or aggressiveness of the individual's disease.

Large regions averaging 55 mm^2 were imaged with CODEX as previously described (Schürch et al. 2020; Phillips, Matusiak, et al. 2021; Hickey et al. 2021)**.** Regions were selected to capture islets and the surrounding region simultaneously (Figure 1.A, center and right). CellSeg was used to segment cell nuclei and quantify marker expression from CODEX images as previously described (Lee et al. 2022)**.** In total, our dataset consisted of $7.0x10^6$ cells across all donors (ranging from $3.0x10^5$ to $9.8x10^5$ cells per donor). Twenty-one cell types were identified with Leiden clustering and manual merging and visualized using Uniform Manifold Approximation and Projection (UMAP) (Figure 1.B, Supplemental Table 2). Endocrine cells were manually gated from UMAP embeddings derived from Proinsulin, Glucagon, and Somatostatin to identify b-cells, a-cells, and d-cells respectively. Immune cells were sub-clustered with the Leiden algorithm using immune-specific markers (Figure 1.C, Supplemental Table 2). To verify the accuracy of our annotations,

we overlaid labelled data onto the original images (Supplemental Figure 1.A). Of note, we could not accurately identify macrophage subsets or distinguish dendritic cells from macrophages due to the panel design, complex combinations of co-expression, and the difficulty in segmenting and quantifying markers on myeloid populations due to their morphology. Therefore, we refer to this cluster as "macrophage/DCs" In addition, we identified a cell population that could not be definitively annotated, expressing high levels of CD45, CD69, Granzyme-B, and CD44, intermediate levels of CD16, S100A6, Galectin-3, and Hyaluronan, but not expressing CD3, CD20, CD56, CD57, CD15, or MPO. We confirmed from the raw images that CD3, CD4, and CD8 were not internalized, indicating activation, nor did these cells express other T cell activation markers CD45RA, CD45RO, PD-1, or LAG-3 (Figure 1.C, Supplemental Figure 1A, bottom right). This population could represent a type of innate lymphoid cell (Dalmas et al. 2017) and was labeled "Granzyme-B$^+$/CD3-".

Islet- and extra-islet regions are altered in T1D

We first sought to identify cellular changes in T1D within islets specifically. Previous reports observed that insulin-containing islets are significantly more common in recent-onset T1D cases than cases with diabetes durations of greater than one year (In't Veld 2011; Campbell-Thompson et al. 2016; Richardson and Pugliese 2022). Similarly, we found that samples from patients who had been diagnosed with T1D for 0-2 years had significantly reduced β-cell frequencies compared to non-T1D controls. Furthermore, samples from subjects with disease durations of 5-6 years had minimal remaining β-cell mass (Figure 1.D). Whereas one AA+ case had β-cell mass comparable to those of cases with disease duration of 0-2 years, the other AA+ case was comparable to non-T1D controls (Figure 1.D). The total islet area imaged was comparable across all donors (Supplemental Figure 1.B).

Next, we investigated how the abundances of non-endocrine cell types inside islets differed across donors. We performed Principal Component Analysis (PCA) on the donors using the frequencies of non-endocrine cell types located in islets. Donors were clearly separated into two groups by the first two principal components; one group included all T1D cases and one AA+ case and the second included all non-T1D cases and the other AA+ case (Figure 1.E). In this analysis, we did not consider β-cells, α-cells, and δ-cells. Thus, donors were stratified by disease duration strictly according to the abundances of immune and other pancreatic, non-endocrine cell types in the islets.

We next considered only cells located outside islets. Again, donors were clearly separable by the first two principal components (Figure 1.F). The first principal component separated cases with times since diagnosis between 0-2 years from non-T1D, AA+, and cases with diabetes durations of 5-6 years (Figure 1.F). The second principal component separated cases with diabetes durations of 5-6 years from the rest (Figure 1.F). Therefore, both the islet and extra-islet spaces of T1D and non-T1D cases were distinct.

Many cell types were increased in T1D cases with times since diagnosis of 0-2 years relative to non-T1D controls (Supplemental Figure 1C). In T1D cases with times since diagnosis of 5-6 years, the abundance of different cell types either remained higher than non-T1D controls or returned to baseline (Supplemental Figure 1.C). This trend was present in both islet and extra-islet regions.

These data demonstrate that the immune activity between the islet and extra-islet compartments are coordinated.

Pseudotemporal reconstruction of islet pathogenesis identifies a conserved trajectory of insulitis

In human T1D, β-cell destruction does not occur simultaneously across all islets and even neighboring islets can be at different stages of destruction (In't Veld 2011; 2014; Damond et al. 2019). We therefore used pseudotime analysis to infer the most likely progression of a single islet through disease space (Damond et al. 2019). To develop a pseudotemporal map, we quantified the cellular composition of each islet, including cells within 20 µm of the islet's boundary, and applied the pseudotime algorithm PArtition-based Graph Abstraction (PAGA) (Figure 2.A; Figure 2.B), (Wolf et al. 2019). PAGA was selected because it is a high-performing algorithm able to identify multiple trajectories, if they exist, while making minimal assumptions about the true structure (Saelens et al. 2019).

Displayed in Figure 2.B is the PAGA force-directed layout where each point represents an islet. Each islet's color reflects the pseudotemporal distance from the centroid of non-T1D islets. As expected, the islets from different donor groups (no T1D, AA+, T1D) had different distributions across the PAGA map (Figure 2.C). In the PAGA map, a continuum is apparent from islets abundant in insulin-expressing β-cells on the left of the map to islets depleted in β-cells on the right (Figure 2.D, Figure 2.E, Figure 2.F, top row). PAGA uses Leiden clustering internally, enabling the following regions of the pseudotime map to be labelled objectively: 1) Islets with low pseudotime values on the left of the map (PAGA-internal Leiden clusters 0 and 5 in Supplemental Figure 2.A) were labelled "Normal" even if they originated from T1D donors. 2) Islets in the middle of the map (PAGA-internal Leiden clusters 6, 2, and 8 in Supplemental Figure 2.A) were elevated in HLA-ABC (MHC Class I) expression, $CD8^+$T cells, and macrophage/DCs (Figure 2.D, Figure 2.E, Figure 2.F, rows 2-4) and were labelled "Inflamed". 3) Islets with late pseudotime values on the right of the map (PAGA-internal Leiden clusters 1,3,7, and 4 in Supplemental Figure 2.A) were devoid of β-cells and were labelled "Insulin-Depleted" (Figure 2.D, Figure 2.E, Figure 2.F, top row).

In addition, islets lacking β-cells occasionally contained $CD8^+$T cells and were labelled "Insulin-Depleted + Immune Islets" (Figure 2.D, Figure 2.E, Figure 2.F, rows 2-4). The presence of these islets suggests that signals retaining $CD8^+$T cells in islets linger after β-cells die. The distribution of all cell types across pseudotime is reported in Supplemental Figure 2.B.

Islets from non-T1D controls and one of the AA+ donors (6314) were primarily in the Normal group to the left of the map (Figure 2.C , Supplemental Figure 2.C). Islets from subjects who had had T1D for of 5-6 years (cases 6195 and 6323) were primarily in the Insulin-Depleted group to the right of the map (Figure 2.C , Supplemental Figure 2.C). All the remaining T1D donors and the other AA+ donor were distributed broadly throughout the map (Figure 2.C , Supplemental Figure 2.C).

We quantified the fraction of each cell type in swaths at varying distances from the islet edge. We found that for B Cells, $CD4^+$T cells, $CD8^+$T cells, macrophage/DCs, neutrophils, and plasma

cells, the fraction of the given cell type in the islet relative to outside the islets increased (Supplemental Figure 2.D), demonstrating that the inflammation in islets was distinct from the inflammation in the extra-islet tissue. Thus, immune cells were targeting islets specifically.

Together, these results illustrate a single, non-branching progression from Normal Islets to Insulin-Depleted Islets via Inflamed Islets, consistent with previous pseudotime analyses (Damond et al. 2019).

IDO expression on islet vasculature is linked to T cell infiltration

We observed islets with vasculature staining positive for indoleamine 2, 3-dioxygenase 1 (IDO). In the tumor microenvironment, IDO is commonly expressed by myeloid cells and suppresses $CD8^+$T cell activity through multiple mechanisms including the induction of $FOXP3^+$ regulatory T cells and the inhibition of $CD8^+$T cell function (Munn and Mellor 2016). In islets, IDO co-stained with $CD31^+$ vasculature but not $CD45^+$ immune cells adjacent to vasculature (Figure 2.G). IDO was not expressed by endocrine or other cell types in islets or by vasculature or any cell type outside islets (Supplemental Figure 2.E). We manually quantified vascular expression of IDO on islets throughout pseudotime and found that all but two IDO^+ islets were in the Inflamed group (Figure 2.H). Therefore, IDO expression by islet vasculature was tightly associated with insulitis.

A potent inducer of IDO expression is Interferon-γ (IFN-γ), a cytokine highly expressed by activated T cells and macrophages (Munn and Mellor 2016). Therefore, we hypothesized that IDO expression was induced by infiltrating immune cells during insulitis. We compared the frequency of $CD8^+$T cells and macrophage/DCs in islets from the Inflamed group with and without IDO^+ vasculature and found that $CD8^+$T cells were significantly more abundant in islets with IDO^+ vasculature than islets without IDO+ vasculature (Figure 2.I). However, the abundance of $\gamma\delta$-T cells and $CD4^+$T cells was less strongly associated with IDO+ vasculature and the abundance of macrophage/DCs was not significantly associated with IDO^+ vasculature (Supplemental Figure 2.F).

In summary, IDO expression by islet vasculature is positively associated with T cell infiltration and may be an immunoregulatory checkpoint.

Insulitis has sub-states, defined by functional states of $CD8^+$T cells

$CD8^+$T cells are a major component of insulitis (row 4 of Figure 2.E and Figure 2.F) and are capable of directly and indirectly killing β-cells. A comprehensive description of the activation profiles of $CD8^+$T cells could provide insight into their roles in T1D pathogenesis. To obtain extremely high-quality marker quantification, we trained a neural network on manually labelled images of single T cells (Figure 3.A, Supplemental Figure 3.A). Using our neural network, we quantified the expression of T cell markers on islet $CD8^+$T cells (Figure 3.B).

PD-1, TOX, CD45RO, CD69, and CD44—markers of antigen experience—were the most commonly expressed by islet-infiltrating CD8$^+$T cells (Figure 3.B, Supplemental Figure 3.B). CD8$^+$T cells expressing CD45RA (which are either naïve or terminally differentiated effector memory cells (TEMRA)) were detectable in islets, as previously reported (Damond et al. 2019) (Figure 3.B). In addition, we observed a rare population of CD45RO$^+$ CD8$^+$T cells co-expressing Lag-3, Granzyme-B, and ICOS (Figure 3.B bottom clade). Lastly, a rare population of CD57$^+$ CD8$^+$T cells was present but these cells rarely co-expressed LAG-3, Granzyme-B, or ICOS (Figure 3.B top clade). These populations resemble the two exhausted T cell populations identified in the peripheral blood of T1D patients that were associated with responsiveness to alefacept (Diggins et al. 2021). Therefore, the activation profiles of islet-infiltrating T cells are heterogeneous.

We reasoned that the islet microenvironment may dictate the activation state of CD8$^+$T cells by specifically recruiting T cells of a particular state and/or inducing changes after they enter the islet. If so, islets would contain specific combinations of CD8$^+$T cell states. To interrogate this, we performed UMAP only on Inflamed islets, using the frequencies of CD8$^+$T cells expressing each functional marker. We identified four inflamed sub-clusters, I-IV, (Figure 3.C top). Here, the term "sub-cluster" is used to highlight that these groups were all contained within the previously defined "Inflamed" cluster and the roman numerals do not imply a temporal ordering. Inflamed-I contained only CD8$^+$T cells that did not express any of the functional markers analyzed (Figure 3.C bottom, top row). Inflamed-II was characterized by a high frequency of CD45RA$^+$CD8$^+$T cells (Figure 3.C bottom, second row from top and Figure 3.D top row). Inflamed-III was characterized by a low frequency of CD45RA$^+$ cells and high frequency of CD45RO$^+$ and PD-1$^+$ cells (Figure 3.C bottom, third row from top and Figure 3.D middle row). Inflamed-IV was characterized by an enrichment of CD8$^+$T cells expressing CD57, LAG-3, ICOS, Granzyme-B, PD-1 or CD45RO (Figure 3.C bottom, bottom row and Figure 3.D bottom row). In summary, the phenotypes of CD8$^+$T cells are coordinated across islets.

Regulation of insulitis sub-states by the islet microenvironment

To identify cellular or molecular factors that regulate the state of CD8$^+$T cells in islets, we first inspected the distribution of inflamed sub-clusters in each patient. Each donor possessed islets that belonged to multiple inflamed islet sub-clusters (Figure 3.E). Therefore donor-level factors such as genetics, the location within the pancreas (i.e. head, body, or tail), or time since T1D onset, are not associated. Instead, these insulitis sub-states are conserved among T1D patients.

Next, we asked if each T cell marker is enriched in CD8$^+$T cells in islets compared to CD8$^+$T cells in the peri-islet and exocrine space. We computed the frequencies of each CD8$^+$T cell state inside islets of each inflamed sub-cluster and in separate swaths 0-25µm, 25-50µm and 50-100µm away from the islets (Supplemental Figure 3.C). We found that for islets of Inflamed-II, -III, and -IV, functional markers characterizing their CD8$^+$T cells were expressed more frequently inside than in the surrounding tissue areas. Although the different functional markers were all enriched on islet-infiltrating T cells compared to T cells outside islets, the degree of this enrichment varied across the markers measured. The markers of Inflamed-IV, LAG-3, ICOS, and Granzyme-B, were

highly enriched inside islets (~20% of islet-infiltrating CD8$^+$T cells vs <5% of extra-islet CD8$^+$T cells). CD45RA and CD69 in Inflamed-II were slightly less enriched in islets (~28% of islet-infiltrating and ~20% of extra-islet CD8$^+$T cells). CD45RO and PD-1 in Inflamed-III islets were the most abundant but had the least enrichment in islets (~45% of islet-infiltrating CD8$^+$T cells vs ~35% of extra-islet CD8$^+$T cells) (Supplemental Figure 3.C). This demonstrated that the specific differences in the compositions of CD8$^+$T cell states in different islets were attributable to the islet microenvironment and not the surrounding extra-islet spaces.

Although macrophage/DCs are abundant in islets from the Inflamed group (Figure 2.E, Figure 2.F) and are capable of interacting with T cells through antigen presentation and cytokine secretion, neither the expression of markers of macrophage/DC activity nor macrophage/DC abundance was significantly associated with any of the inflamed sub-clusters (Supplemental Figure 3.D). Similarly, no other cell-type nor the vascular expression of IDO was linked to CD8$^+$T cell programs in islets (Supplemental Figure 3.D). Accordingly, the four inflamed sub-clusters had identical distributions throughout the original PAGA force-directed layout (Figure 3.F). Therefore, the activation states of islet-infiltrating T cells are independent of the abundance of any of the other cell types we could identify.

Lastly, we compared CD8$^+$T cells in islets from the Insulin-Depleted + Immune group to CD8$^+$T cells in islets from the Inflamed group. Insulin-Depleted + Immune islets contained a higher frequency of CD45RA+ CD8$^+$T cells and a lower frequency of CD45RO+ CD8$^+$T cells than Inflamed islets (Figure 3.G). TOX was expressed by a higher frequency of CD8$^+$T cells in Insulin-Depleted + Immune islets than CD8$^+$T cells in Inflamed islets (Figure 3.G). Importantly, CD45RA+ and TOX were never co-expressed on the same CD8$^+$T cell (Figure 3.B). These data indicate that the activation state or persistence of these two populations in islets depends on insulin expression.

Vasculature, nerves, and Granzyme-B$^+$/CD3- cells outside islets are associated with lobular patterning

The destruction of islets in T1D is known to exhibit lobular patterning: that is, islets in the same lobule are likely to be in the same stage of disease (Gepts 1965). The reason why islets within the same lobule are synchronized is unknown. One explanation could be an islet-intrinsic mechanism where the expression of programs sensitizing beta cells to immune-killing (i.e. stress) are correlated across islets in the same lobule. Alternatively, it could be mediated by cells outside islets if they facilitate extravasation into the lobule or trafficking from one afflicted islet to the next.

To systematically investigate lobular patterning in T1D, we used a neural network to segment lobules and assign each single cell and islet, to its lobule. We first quantified the degree of lobular patterning within each donor using the intra-class correlation coefficient (ICC). The ICC ranges from 0 to 1 where cases with values closer to 1 have islets whose states are more synchronized within lobules (Figure 4.A). Islets of non-T1D cases and 6314, 6195, and 6323 did not have appreciable variability in their pseudotimes, but in the remaining cases, the ICCs ranged from 0.17 to 0.74 (Figure 4.B). This highlights that the magnitude of lobular patterning ranges widely across T1D cases with insulitis.

We employed hierarchical linear modeling (HLM), a statistical framework designed to identify relationships between levels of multi-level data. HLMs are standard in fields where multi-level data are common such as Education, in which students are grouped into classrooms, which are grouped into schools (Gelman et al. 2014) and have been applied in biomedical settings (Jerby-Arnon and Regev 2022; Yi et al. 2019). We were interested in cell-types if their abundance in a lobule correlated with the lobule's average islet pseudotime. Importantly, we omitted the islet region itself from the calculation of a cell type's lobular abundance because we were interested in identifying features in the extra-islet space that were associated with islet destruction. For each cell type, we estimated the effect of its total abundance in a lobule (the number of cells divided by the number of acinar cells to normalize for lobule area) on the pseudotimes of islets in that lobule. We performed this analysis in two-level HLMs for each donor and a three-level HLM considering all donors together (Figure 4.C).

We identified three cell types, vasculature, Granzyme-B$^+$/CD3- cells, that were significantly associated with lobules across multiple T1D tissue donors. All three were more abundant in lobules with islets late in pseudotime (Figure 4.C boxed rows, Figure 4.D). Samples from cases 6323 and 6195 which had very few insulin-containing islets had increased abundances of vasculature, Granzyme-B/CD3- cells, and nerves in their extra-islet spaces compared to non-T1D controls (Supplemental Figure 1C), indicating these changes persist through the point when the entire tissue is afflicted. In addition, vasculature, Granzyme-B$^+$/CD3- cells, and nerves were increased in Inflamed islets compared to Normal islets indicating that they may serve a role in islets in addition to their role in the extra-islet compartment (Supplemental Figure 4A). Note that Supplemental Figure 4A differs from Supplemental Figure 1C because islets are broken up according to pseudotime, not donor, and not all islets in T1D donors are undergoing insulitis.

Counterintuitively, although CD8$^+$T cells and macrophage/DCs were higher in the extra-islet compartments of T1D cases vs non-T1D cases (Supplemental Figure 1C), they were not associated with lobular patterning (they were not more abundant in the extra-islet space of lobules with more advanced insulitis) (Figure 4.C). These data raise the possibility that vasculature, Granzyme-B/CD3- cells, and nerves outside islets help predispose lobules to insulitis or are affected by extensive insulitis.

Immature tertiary lymphoid structures are enriched in subjects with T1D

We hypothesized that T cells' interactions with certain cell types in specific areas of the pancreas may be important for their functionality. Therefore, we identified Cellular Neighborhoods (CNs) (Schürch et al. 2020; Bhate et al. 2021), tissue regions that are homogeneous and have defined cell-type compositions. To identify CNs, single cells were clustered according to the cell-type composition of their twenty nearest spatial neighbors and automatically annotated with the names of enriched cell types using (Figure 5.A, See Methods). This resulted in 75 CNs. Throughout the manuscript, CNs are referred to with the nomenclature (Cell Type A|Cell Type B|…) to indicate all the cell types that are enriched in them (See Methods).

Next, we identified CNs that were more abundant in T1D than non-T1D tissues (Figure 5.B). The top three CNs (fold change of abundance in T1D relative to abundance in non-T1D) were (CD8$^+$T cells|B Cells), (Macrophage|Stromal Cells|B Cells), and (Vasculature|B Cells) (Figure 5.B, Figure 5.C). We asked whether these three CNs were commonly adjacent to each other as this could indicate that they act as components of a larger structure (Bhate et al. 2021). Measuring the frequency with which the three B cell CNs were adjacent to each other throughout the tissues demonstrated that the (CD8$^+$T cells|B Cells) CN is predominantly found adjacent to both the other CNs but that (Macrophage|Stroma|B Cells) and (Vasculature|B Cells) are less commonly adjacent to each other (Figure 5.D).

We next asked whether these CN assemblies corresponded to either peri-vascular cuffs (Agrawal et al. 2013; Wekerle 2017) or tertiary lymphoid structures (TLSs) (Korpos et al. 2021; Rovituso et al. 2016; Agrawal et al. 2013), as these are two B Cell-rich structures commonly present in autoimmune conditions. Although the (CD8$^+$T cells|B Cells) CN was adjacent to vessels (Figure 5.D, Figure 5.E), it was not in the fluid-filled perivascular space, as is the case with perivascular cuffs (Figure 5.E). In our samples, the (CD8$^+$T cells|B Cells) CN did not have segregated T cell and B cell zones as seen in mature TLSs, consistent with (Korpos et al. 2021).

In summary, the (CD8$^+$T cells|B Cells) CN is more abundant in T1D tissues from patients with diabetes durations of 0-2 years compared to non-T1D tissues and T1D tissue from patients who had T1D for more than 4 years.

Immature tertiary lymphoid structures are in the extra-islet pancreas, and are enriched in CD45RA$^+$/CD8$^+$ T cells

We next asked whether the (CD8$^+$T cells|B Cells) CN had high endothelial venules (HEV), specialized blood vessels that are commonly found in TLSs that enable naïve lymphocytes to extravasate into peripheral tissues. We observed expression of peripheral lymph node addressin (PNAd), an HEV marker, in the vessels associated with the (CD8$^+$T cells|B Cells) CN (Figure 5.E left image) but not in other vessels (data not shown). Although we could not assess the presence of other TLS traits such as follicular dendritic cells, fibroblastic reticular cells, or follicular helper T cells, the aggregation of B cells and presence of HEVs, but the lack of compartmentalized B and T cell zones indicate that instances of the (CD8$^+$T cells|B Cells) CN are immature TLSs.

Next, we asked if immature TLSs could support the entry of naïve CD8$^+$T cells into the pancreas. We observed CD8$^+$T cells co-expressing CD45RA and CD62L (the ligand for PNAd) near PNAd$^+$ vasculature (Figure 5.E, middle and right image respectively). Thus, CD45RA$^+$/CD8$^+$T cells in the pancreas can adhere to HEVs. Furthermore, CD45RA$^+$ was enriched three-fold on CD8$^+$T cells in the (CD8$^+$T cells|B Cells) CN relative to CD8$^+$T cells in the tissue as a whole (Figure 5.F), providing additional evidence that CD45RA+ T cells may enter the pancreas through HEVs.

We found immature TLS both adjacent (Figure 5.G.1) or not adjacent (Figure 5.G.2) to islets. Quantifying the frequency of this adjacency revealed that fewer than half of the immature TLS were adjacent to islets (Figure 5.H). We did not identify any differences in the cellular composition of the immature TLS that were or were not adjacent to islets (Supplemental Figure 5). We reasoned that even if immature TLSs were far from islets, extravasating cells may migrate

to islets. Accordingly, islet-adjacent CD45RA$^+$ CD8$^+$T cells (that were not in islet-adjacent TLSs) co-expressed CD62L, suggesting that they originated from the (CD8$^+$T cells|B Cell) CN (Figure 5.I). Consistent with this, in one notable tissue donor, regions of the pancreas with Insulin-Depleted islets were enriched in the (CD8$^+$T cells|B Cell) CN relative to regions of the pancreas with β-cell containing islets (Figure 5.J). This spatial correlation between the (CD8$^+$T cells|B Cells) CN and the destruction of islets implicates immature TLS with islet pathology even if they are not adjacent to islets (Figure 5.J).

Discussion

We have performed CODEX imaging and comprehensive computational analysis of whole cadaveric pancreata from T1D subjects. Our data support several conclusions.

First, our results are consistent with the model previously proposed by Damond et al, who proposed a single trajectory for insulitis, characterized by an enrichment in HLA-ABC expression, CD8$^+$T cells, and macrophage/DCs (Damond et al. 2019).

Second, we are the first to report that IDO+ vasculature is present in inflamed islets but not in normal islets or islets that have lost insulin-expression (Figure 2.G,Figure 2.H). Furthermore, islets with IDO+ vasculature contained higher frequencies of CD8$^+$T cells, but not macrophage/DCs compared to inflamed islets that did not contain IDO+ vasculature, suggesting that IDO is induced by a cytokine produced by infiltrating CD8$^+$T cells such as IFN-γ (Figure 2.I). Given IDO's established tolerogenic role, these data suggest that the loss of IDO on vasculature could be a prerequisite for β-cell death. Leveraging this checkpoint to protect transplanted β-cells from rejection has shown promise (Alexander et al. 2002) and could be combined with similar approaches using programmed death-ligand 1 (Yoshihara et al. 2020; Castro-Gutierrez et al. 2021)

We did not observe IDO expression on β-cells, in contrast to Anquetil et al. that report this in healthy patients (Anquetil et al. 2018). Our observations are consistent with data demonstrating that IDO needs to be induced. First, it has been shown with western blot and RT-PCR that human islets require cytokine stimulation to express IDO (Sarkar et al. 2007). Second, the human protein atlas has tested multiple IDO antibodies and demonstrated that IDO is negative in human islets via immunohistochemistry: (https://www.proteinatlas.org). In addition, the human protein atlas's single-cell RNAseq atlas only report IDO transcripts in immune cells in healthy pancreas.

Third, we performed the first high-dimensional spatial phenotyping of CD8$^+$T cells in T1D islets. We found that most T cells were antigen experienced. A small population expressed CD45RA and CD69, which could be naïve or TEMRA cells (Figure 3.B). Another population expressed Lag-3, Granzyme-B, and ICOS. It is notable that only a small population of islets had Granzyme-B-expressing T cells. This could indicate that alternative mechanisms are contributing to the elimination of β-cells.

Fourth, the insulitis trajectory is comprised of four sub-clusters, each characterized by the activation profile of the islet-infiltrating CD8+T cells (Figure 3.C). Multiple of these inflamed sub-clusters were present in all T1D donors, indicating that the sub-clusters are capable of inter-converting (Figure 3.E). The factors that regulate the conversion of a given islet between sub-

clusters could correspond to immunoregulatory checkpoints that are critical to the progression of T1D. Unfortunately, our search for such features failed to generate any candidates (Supplemental Figure 3.D). By phenotyping T cells at different distances from the islet edge, we were able to determine that the T cell activation profiles characterizing each sub-cluster were only present in the islet, not in the surrounding tissue (Supplemental Figure 3.C). Unfortunately, from our data, we cannot speculate whether the insulitis sub-clusters arose due to differential stimulation of T cells that had already entered islets, differential recruitment of pre-activated T cells, or both.

Fifth, pancreatic lobules affected by insulitis are characterized by distinct tissue markers. We discovered that lobules enriched in β-cell-depleted islets were also enriched in nerves, vasculature, and Granzyme-B$^+$/CD3- cells, suggesting these factors may make lobules permissive to disease (Figure 4.C). The role of islet enervation in T1D has been studied but such work has focused on nerves in the islet rather than on nerves in the exocrine tissue (Christoffersson, Ratliff, and von Herrath 2020). The Granzyme-B+/CD3- cells could be natural killer cells; if so, they are most likely of the CD56dim subset as CD56 was not detected on these cells. It is noteworthy that the cell types linked with direct islet invasion were distinct from those linked to lobule patterning even though both sets of cell types were found across islet and extra-islet regions. Therefore, for insulitis to consume every islet, crosstalk may be required between the cell types in the islet and extra-islet compartments. Conversely, inhibiting this interaction might contain pathology to isolated lesions.

Finally, we identify immature TLS away from islets where CD45RA$^+$ CD8$^+$T cells aggregate. We also observed an inflamed islet-subcluster characterized by an abundance of CD45RA$^+$/CD8$^+$ T cells. It will be important to determine whether the CD45RA$^+$ T cells localized around islets may have originated from immature TLS. In mice, blocking immune egress from lymph nodes reduced the size of TLSs and halted diabetes (Penaranda et al. 2010). Thus, therapeutic targeting of immune cell trafficking to TLS could help mitigate autoimmunity in human T1D.

Together, these data illuminate relationships between insulitis, the local islet microenvironment and inflammation at distal sites.

A major limitation for the study is the cohort size. Cases with documented insulitis are very rare, significantly limiting the feasibility of curating large cohorts (Campbell-Thompson et al. 2016). Due to this limitation, factors such as the donors' histories of drug use, durations of stay in the intensive care unit, and BMIs could not be balanced or statistically adjusted for but should be considered when relevant and are associated with exocrine inflammation but not the prevalence of insulitis (Bruggeman et al. 2021). In addition, only one of the AA+ cases, Case 6267, had detectable insulitis (Figure 2.C). The other case, 6314 tested positive for only one autoantibody, GADA+, and therefore had a significantly lower probability of progressing to overt T1D (Ziegler et al. 2013).

Another limitation is our limited perspective on myeloid cell populations. Although antibodies in our panel detect numerous myeloid markers, we failed to identify any heterogeneity in myeloid populations during insulitis. This was likely due in part to the difficulty of segmenting myeloid cells and quantifying marker expression due to their morphology. Spatial transcriptomics could

be used in future studies to better define the myeloid populations and inform additions to future CODEX panels.

Lastly, our samples are 2-dimensional sections which could affect some of the adjacency relations.

In conclusion, using a data-driven approach, we mapped conserved sub-states of insulitis and integrated the spatial pathology of islet and extra-islet regions into a single model of T1D pathogenesis. The tools and computational pipelines developed here will enable further investigation of immune pathology at the tissue scale that may lead to development of therapies for T1D.

Methods

Human tissues

Cadaveric pancreatic FFPE tissue sections were obtained through the nPOD program, sponsored by the Juvenile Diabetes Research Fund. Case numbers cited herein are assigned by nPOD and comparable across nPOD-supported projects. 17 cases in the nPOD biorepository had been previously documented to contain insulitis. For each of these 17 cases, we examined the triple stained immunohistochemistry images (CD3, Insulin, and Glucagon) using nPOD's online pathology database to select blocks in which insulitis was present. To ensure that the tissue regions still contained insulitis (and had not been sectioned extensively after their images were uploaded to the nPOD pathology database), we re-sectioned and visualized CD3, Insulin, and Glucagon. The use of cadaveric human tissue samples is approved by Stanford University's Institutional Review Board.

CODEX data collection

CODEX Antibody Generation and Validation. Oligonucleotides were conjugated to purified, carrier-free, commercially available antibodies as previously described (Schürch et al. 2020; Kennedy-Darling et al. 2021). For validation experiments, human tonsils and non-diabetic pancreata were co-embedded in FFPE blocks so both tissues could be stained and imaged simultaneously. Each antibody in the CODEX panel was validated by co-staining with previously established antibodies targeting positive and negative control cell types. Once validated, the concentration and imaging exposure time of each antibody were optimized. The tissue staining patterning was compared to the online database, The Human Protein Atlas, and the published literature. The specificity, sensitivity, and reproducibility of CODEX staining has been previously validated (Schürch et al. 2020; Kennedy-Darling et al. 2021; Black et al. 2021; Phillips, Schürch, et al. 2021; Phillips, Matusiak, et al. 2021)

CODEX Staining. Staining and imaging was conducted as previously described (Schürch et al. 2020; Kennedy-Darling et al. 2021; Phillips, Schürch, et al. 2021; Black et al. 2021). Briefly, FFPE tissues were deparaffinized and rehydrated. Heat-induced epitope retrieval (HIER) antigen retrieval was conducted in Tris/EDTA buffer at pH9 (Dako) at 97°C for 10 minutes. Tissues were

blocked for 1 hour with rat and mouse Ig, salmon-sperm DNA, and a mixture of the non-fluorescent DNA oligo sequences used as CODEX barcodes. Tissues were stained with the antibody cocktail in a sealed humidity chamber overnight at 4°C with shaking. The next day, tissues were washed, fixed with 1.6% paraformaldehyde, 100% methanol, and BS3 (Thermo Fisher Scientific), and mounted to a custom-made acrylic plate attached to the microscope.

CODEX Imaging. Imaging was conducted using the Keyence BZ-X710 fluorescence microscope with a CFI Plan Apo λ 20x/0.75 objective (Nikon). "High resolution" mode was selected in Keyence Navigator software, resulting in a final resolution of .37744 µm/pixel. The exposure times are listed in Supplemental Table 3. Regions for imaging were selected by rendering HLA-ABC, Proinsulin, and CD8 and selecting large regions (averaging 55mm^2). The full antibody panel and cycle-ordering is detailed in (Supplemental Tables 3 and 4). Biotinylated hyaluronan-binding protein was rendered by adding streptavidin-PE at 1:500 concentration to the 96 well plate containing fluorescent oligos in the last cycle and running the CODEX program normally. DRAQ5 was added to the last cycle because we found it stained nuclei more evenly than HOECHST which slightly improved segmentation. Each tissue took between 3 and 7 days to image depending on the tissue area.

Characterization of Tertiary Lymphoid Structures. A serial section from case 6228 was imaged in a separate CODEX experiment using an antibody panel tailored for characterizing tertiary lymphoid structures, as described in Supplemental Table 3. These data were acquired and analyzed identically to the main dataset.

Image Pre-processing. Drift compensation, deconvolution, z-plane selection was performed using the CODEX Toolkit uploader (github.com/nolanlab/CODEX, Goltsev et al. 2018). Cell segmentation using the DRAQ5 nuclear channel and lateral bleed compensation was performed with CellSeg (Lee et al. 2022).

Cell Type Clustering and Annotation

Marker expression was z-normalized within each donor and subsequently clustered in two steps. First, cells were projected into 2 dimensions using the markers indicated in Supplemental Table 2 and Parametric Uniform Manifold Approximation and Projection (pUMAP)(Sainburg, McInnes, and Gentner 2021) was applied on a downsampled dataset. The fit model was used to transform the remaining cells. Cell types were gated using Leiden clustering and manual merging. The cluster containing immune cells was sub-clustered using the markers detailed in Supplemental Table 2. Acinar cells contaminating the Immune cluster were gated out and merged with the Acinar cluster from the previous step. The Endocrine class was sub-clustered into α-, β-, and δ-Cells using Glucagon, Proinsulin, and Somatostatin respectively. Clusters were annotated according the heatmap marker expression, and overlaying annotations onto raw images (Supplemental Figure 1.A) using custom scripts in Fiji.

Islet Segmentation and Pseudotime

Preprocessing. Windows consisting of the twenty nearest spatial neighbors surrounding each single cell were clustered according to their cell-type composition using Mini Batch K Means with k=200. For this analysis, α-, β-, and δ-Cells were combined into one 'Endocrine' cell type. One cluster was highly enriched in Endocrine cells and accurately defined the islet area. Individual islets were identified using the connected components algorithm and filtering out islets that had fewer than ten total cells.

PAGA Analysis. For each islet, the number of each cell type inside the islet and between the islet edge and 20µm beyond were extracted. To adjust for variation due to the islet size, the cell type counts were divided by the number of endocrine cells inside the islet. Data were then log-transformed. The PAGA embedding was computed using the default parameters except for the following: The neighborhood search was performed using cosine distance and 15 nearest neighbors; Leiden clustering used a resolution of 1. For computing the pseudotime values (used in the colormap in Figure 2B, the x-axis in Figure 2F, and Figure 4), the path through the inflamed islet was isolated by temporarily omitting 25 islets positioned in the middle of the map between Normal and Insulin-Depleted islets. Only 9 of these were from T1D or AA+ donors.

Quantification and Validation of Functional Marker Gating

Annotation of Ground-Truth Dataset. 4000 $CD8^+$T cells were labelled for fifteen markers by an immunologist familiar with the staining patterns of each marker using VGG Image annotator (Abhishek Dutta and Andrew Zisserman 2019).

Automated Thresholding. For each functional marker of interest, the lateral-bleed-compensated mean fluorescence (Lee et al. 2022) of cell types known to not express the marker in question were used to calculate a background distribution. Marker-positive cells were defined as those whose expression was greater than the 99^{th} percentile of the background distribution.

Gating with Neural Network: 22µm x 22µm cropped images of each single cell were used as training data. The marker that the image corresponded to was not included as an input in the neural network and one classifier was trained for all markers. Cells were split into training, validation, and test splits (60/15/25 respectively). ResNet50 architecture and initial weights were imported from the Keras library pre trained on ImageNet. Image augmentation consisted of random flips, rotations, zooms, contrast, and translation (+/- ten pixels only). All weights were unfrozen, and the model was trained for 100 epochs (see accompanying source code for training details).

Sub-clustering of Inflamed Islets with Cell-Type specific Functional Markers

For each Inflamed Islet (n=351), the frequency of each marker expressed by $CD8^+$T cells was computed. Single cells inside the islet and within 20µm from the islet's edge were combined before the frequency was measured. The subsequent matrix underwent z-normalization

615 followed by UMAP gating using Bokeh. Insulin-Depleted + Immune Islets were defined as islets
616 without β-cells with greater than two $CD8^+$T cells and greater than seven macrophage/DCs. These
617 thresholds correspond to the 95^{th} percentiles of $CD8^+$T cells and macrophage/DCs in Normal
618 islets.
619

620 ## Identification of Cellular Neighborhoods

621 Previously, CNs (Schürch et al. 2020) were identified by, for each single cell, defining its 'window'
622 as the 20 spatial nearest neighbors. Cells were clustered according to the number of each cell
623 type in their windows using Mini Batch K-Means. The output clusters corresponded to CNs. To
624 ensure our method was sensitive to rare neighborhoods, we adapted this algorithm by
625 intentionally over-clustering, using k=200 in the K- Means step rather than using a k ranging from
626 10-20 as used elsewhere (Bhate et al. 2021; Phillips, Matusiak, et al. 2021; Shekarian et al. 2022).
627 Next, to determine which cell types were characteristic of each cluster, we identified, for each
628 cluster, the set of cell-types that were present in more than 80% of the windows allocated to that
629 cluster. We named the clusters according to this set of cell-types and merged all clusters with the
630 same name, resulting in seventy-five CNs. Acinar cells and epithelial cells were used in the kNN
631 graph and in the clustering but were not considered when merging clusters. Note that this
632 method does not differentiate neighborhoods that have the same combination of cell types but
633 different stoichiometries.

634 ## Lobule Segmentation

635 A training dataset was generated by manually tracing the edges of lobules in ImageJ using the
636 ROI function. The ROI were then floodfilled in Python and used as masks for training. For each
637 tile, the blank cycle was selected to distinguish tissue from background coverslip. A U-Net
638 model was trained for 10 epochs (see attached source code for training details). After stitching
639 together all masks, the resulting images required slight refinement where lobules were not
640 completely separated, and this was done manually in ImageJ. The connected components in the
641 stitched image defined the lobule instances. Cells were assigned to a lobule by indexing the
642 lobule mask with their X and Y coordinates. Cells in the inter-lobular space were assigned to
643 one "edge" lobule. This resulted in 464 lobules.
644

645 ## Formulation of Hierarchical Linear Models

646 For each lobule, the number of each cell type in the extra-islet space was divided by the
647 number of acinar cells in the extra-islet space. For all HLMs, the *lme4* package for R was used
648 (Bates et al. 2015) and statistical significance was computed using the *lmerTest* package for R
649 (Kuznetsova, Brockhoff, and Christensen 2017). Lobular cell-type abundance was z-normalized
650 within each donor and the pseudotime was z-normalized across the entire dataset prior to
651 fitting.
652

653 The ICC was computed using the model: $pseudotime_{islet}$ *~1|loduleID* with the *performance*
654 package in R. A value of 0 indicates that the variation in pseudotimes of islets within the same
655 lobule is equal to the variation across all islets in the donor and a value of 1 indicates that the

variation in pseudotimes of islets within the same lobule is much smaller than that of all islets in the donor.

For each cell type, a two-level, random intercept HLM within each donor was constructed with the following formulation (in R formula syntax): $pseudotime_{islet} \sim celltype_{lobule} + (1|loduleID)$ and a three-level random intercept, random slope HLM including islets from all donors was formulated: $pseudotime_{islet} \sim celltype_{lobule} + (1+celltype_{lobule}|donorID) + (1|loduleID)$. Here, $pseudotime_{islet}$ equals the pseudotime of each islet, $celltype_{lobule}$ equals the number of the given cell type in a particular lobule divided by the number of acinar cells in that lobule, z-normalized within each donor, and *loduleID* and *donorID* are categorical variables specifying the lobule and donor that the given islet belongs to.

Neighborhood Adjacency

The adjacency between neighborhoods was computed as in (Bhate et al. 2021). The only modification was that neighborhood instances were identified using connected components of the k-NN graph with k=5 rather than from the thresholded images.

Data Availability

Processed single cell dataframes are accessible at:

https://www.dropbox.com/sh/8sqef3iwjb6f4wp/AAAQzFgDOgMBiWh9Jqcb81U8a?dl=0.

The raw and stitched, processed data is hosted by the BioImage Archive (https://www.ebi.ac.uk/bioimage-archive/) with the accession number S-BIAD859.

Code Availability

All primary code is attached with the supplementary information and will be posted on the Nolan Lab's github upon acceptance. The code is completely open source. The code is not intended as a software tool and so no small example data set is applicable.

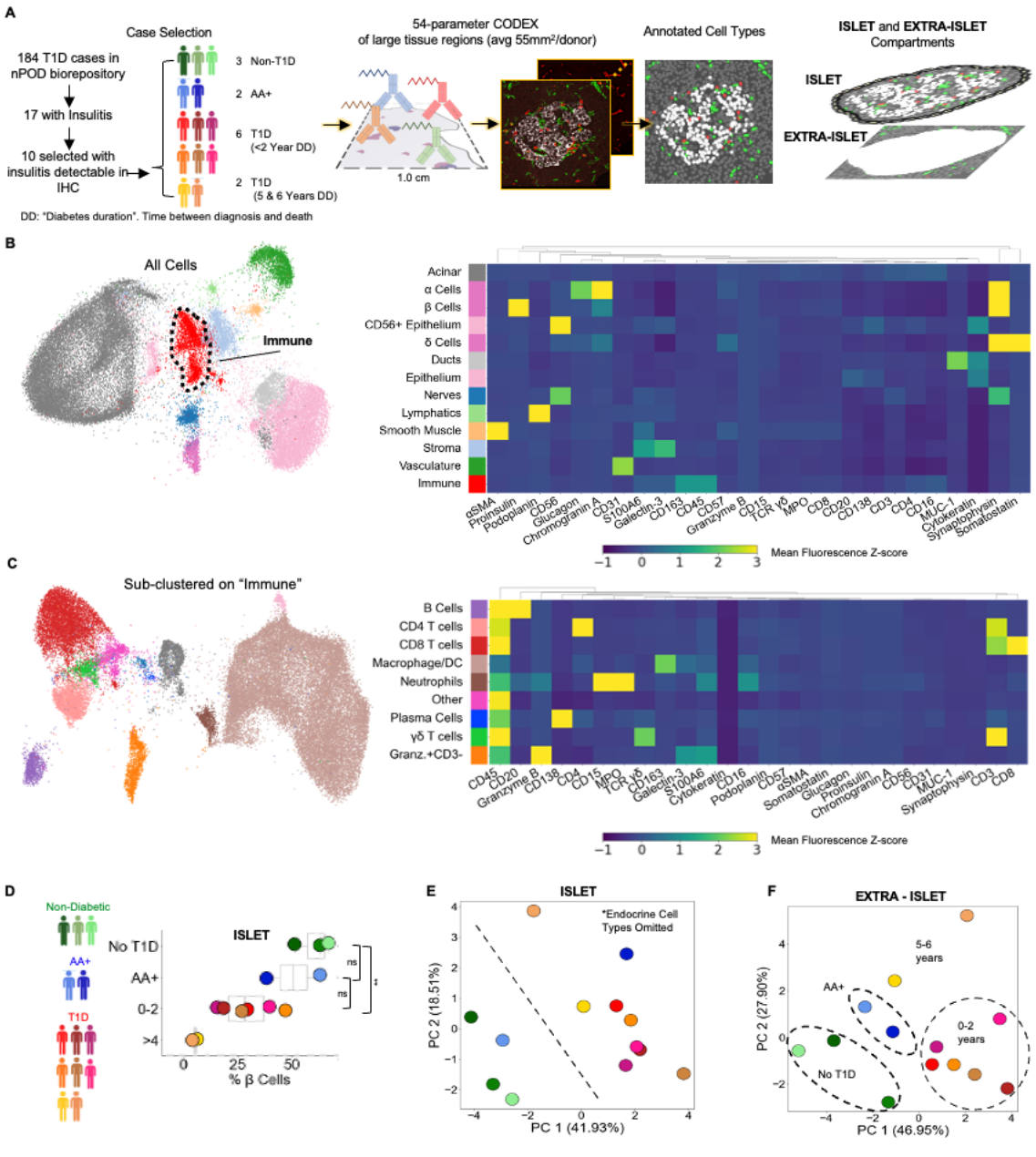

Figure 1 Profiling T1D pancreata with CODEX high-parameter imaging reveals alterations in islet and extra-islet regions.

Figure 1.A Left: Schematic of the workflow for selection of nPOD cases. Blues, greens, and reds indicate non-T1D, AA+, or T1D status, respectively. Center: Schematic for acquisition and processing of CODEX highly multiplexed imaging dataset. Right: Schematic of islet and extra-islet pancreatic regions.

Figure 1.B UMAP and Leiden clustering of major cell types. Colors match those in the heatmap shown to the right. Heatmap of mean z-normalized marker expression in each cell-type cluster. Only a subset of the markers used for the UMAP are included in the heatmap to facilitate

694 visualization. A full description of the markers used for the clustering stages is available in
695 Supplemental Table 2.

696 Figure 1.C UMAP of the immune population identified in Figure 1B further clustered using
697 additional immune markers as described in Supplemental Table 2. Colors match those in heatmap
698 shown in the heatmap to the right. The heatmap is generated in an identical manner as the
699 heatmap in Figure 1B.

700 Figure 1.D Frequency of β-Cells per donor determined by dividing the number of β-cells by the
701 total number of β-cells, α-cells, and δ-Cells. Blues, greens, and reds indicate non-T1D, AA+, or
702 T1D status, respectively. Significance was determined using the t-test (* $p<0.05$, ** $p<0.01$, ***
703 $p<0.001$)

704 Figure 1.E Principal component analysis of the islet compartment. The number of cells of each
705 cell type (omitting α-, β-, and δ-cells) were divided by the number of endocrine cells to adjust for
706 different islet areas. Blues, greens, and reds indicate non-T1D, AA+, or T1D status, respectively.

707 Figure 1.F Principal component analysis of the extra-islet compartment. The number of cells of
708 each cell type (omitting α-, β-, and δ-cells) were divided by the number of acinar cells to adjust
709 for different areas imaged. Blues, greens, and reds indicate non-T1D, AA+, or T1D status,
710 respectively.

711

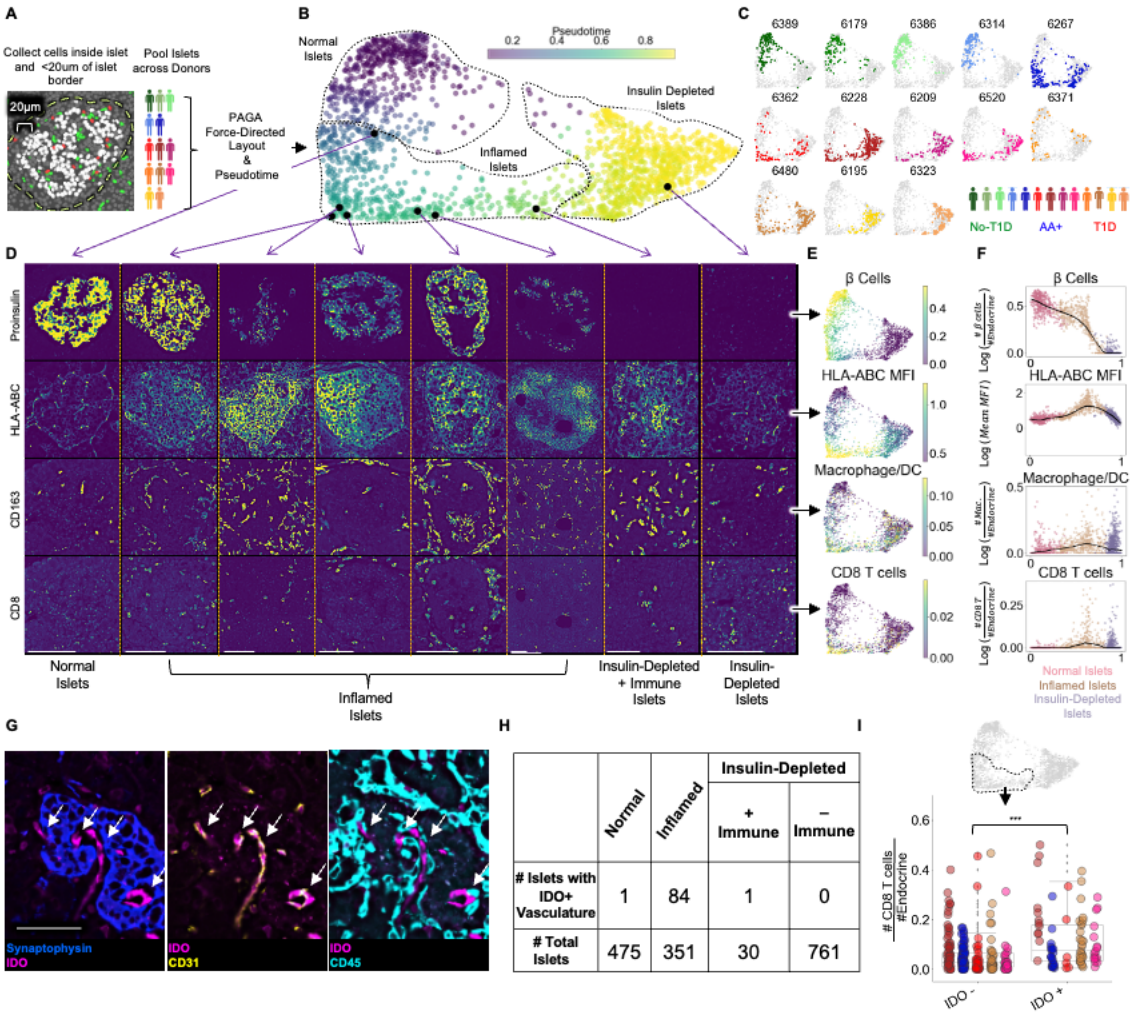

	Normal	Inflamed	Insulin-Depleted	
			+ Immune	– Immune
# Islets with IDO+ Vasculature	1	84	1	0
# Total Islets	475	351	30	761

Figure 2 Pseudotemporal reconstruction of insulitis identifies IDO on islet vasculature.

Figure 2.A Schematic of islet segmentation and quantification of islet cellular composition.

Figure 2.B PAGA-force directed layout of islets colored by pseudotime. The start point of pseudotime was calculated as the centroid of the non-T1D islets. Representative islets from different stages of pseudotime are indicated with black points and their raw images are depicted in Figure 2.D. Normal, Inflamed, and Insulin-Depleted were identified by examining the cell composition of the clusters obtained internally by the PAGA algorithm (Supplemental Figure 2.A).

Figure 2.C Islet distribution across pseudotime for each donor. The titles indicate nPOD case IDs as in Supplemental Table 1. The frequency of islets from each donor in each stage of islet pseudotime is reported in Supplemental Figure 2.C.

Figure 2.D Images of Proinsulin, HLA-ABC, CD163, and CD8 staining in islets representative of different points along pseudotime as indicated in B. Scale bars (lower left of each column) indicate 100µm.

Figure 2.E Quantification of selected features across pseudotime overlaid onto the PAGA force-directed layout. For β-cells, macrophage/DCs, and $CD8^+$T cells, the values correspond to log(# cells/# endocrine cells). For HLA-ABC, the mean HLA-ABC expression for each cell in the islet was computed and log transformed.

Figure 2.F Quantification of selected features across pseudotime. For β-cells, macrophage/DCs, and $CD8^+$T cells, the values correspond to log(# cells/# endocrine cells). For HLA-ABC, the mean HLA-ABC expression for each cell in the islet was computed and log transformed. Color legend: Normal islets: pink; Inflamed islets: brown; Insulin-Depleted islets: purple. Black points demarcate LOWESS regression.

Figure 2.G Representative image of an islet from the Inflamed group stained with IDO and, from left to right, Synaptophysin, CD31, and CD45. Arrows indicate $IDO^+/CD31^+$ vasculature. Right shows that IDO^+ cells are negative for CD45 and therefore, are not myeloid cells associated with vasculature. Scale bar (bottom left image) indicates 50 μm.

Figure 2.H Distribution of IDO expression on islet vasculature across pseudotime.

Figure 2.I Association of IDO^+ islet vasculature with islet $CD8^+$T cell density. The y-axis corresponds to the number of $CD8^+$T cells per endocrine cell per islet. $CD8^+$T cell counts were normalized to adjust for islet size. The x-axis indicates whether islets contain IDO^+ vasculature. Each color corresponds to a donor. All donors with detectable IDO^+ Islet vasculature are displayed which consisted of 6480, 6267, 6520, 6228, and 6362. Colors are same as in Figure 2.C. IDO^+ vasculature was manually quantified. For combined donors, significance was determined with a mixed-effect linear model, $p = 1.5 \times 10\text{-}12$ (Satterthwaites's method lmerTest R package). The complete breakdown per donor is reported in Supplemental Figure 2.F.

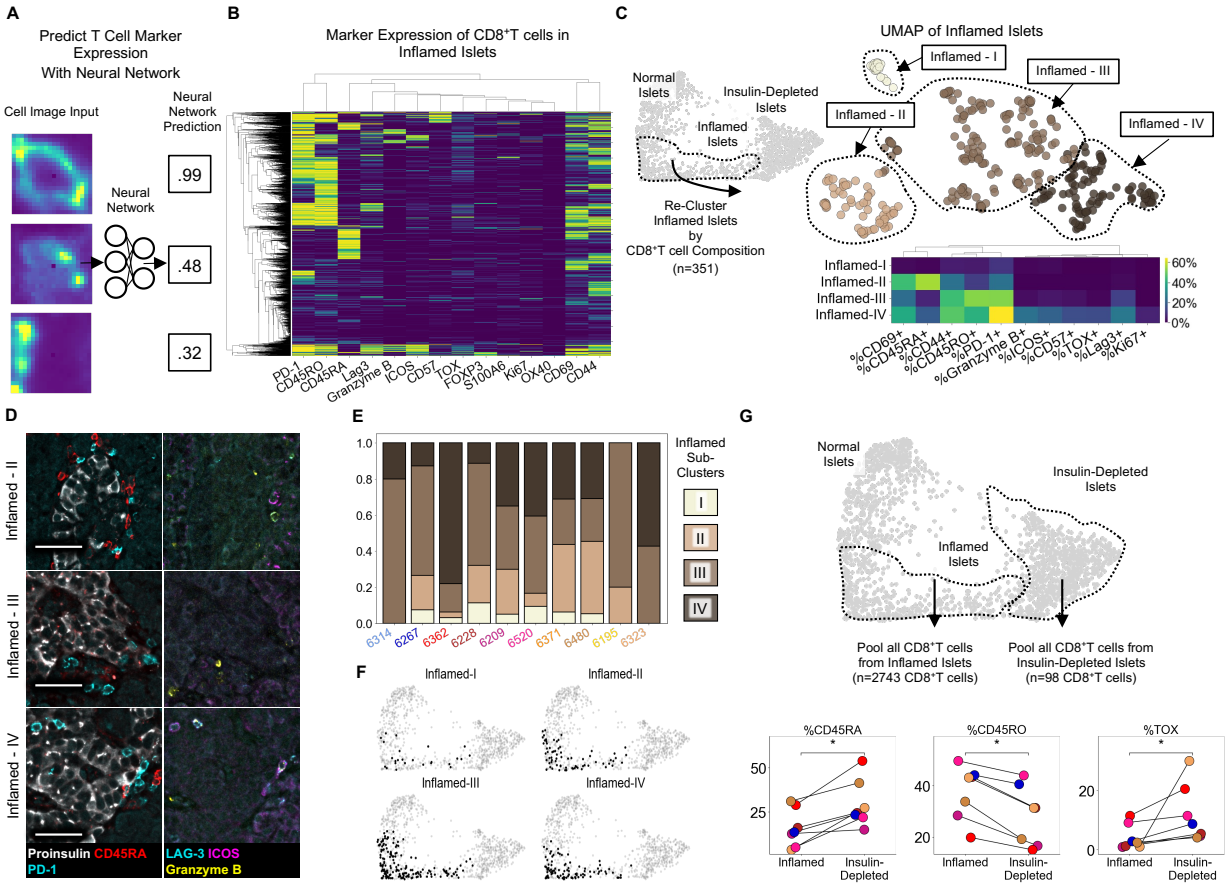

749

Figure 3 Insulitis has sub-states, characterized by CD8⁺T cell functionality

Figure 3.A Schematic of marker-quantification with a ResNet50 neural network. Raw images are input, and the neural network outputs a number between 0 and 1 indicative of the level of confidence that the cell expresses that marker with 1 indicating the highest confidence.

Figure 3.B Heatmap of all 2,855 Inflamed Islet CD8⁺T cells, hierarchically clustered according to marker expression predicted by the neural network.

Figure 3.C Top) UMAP of Inflamed Islets based on frequencies of markers on CD8⁺T cells in islets. Bottom) Mean frequencies of each marker on CD8⁺T cells in islets of each inflamed sub-cluster.

Figure 3.D Representative images of islets from each subcluster with associated immune markers. Scale bars indicate 50 µm.

Figure 3.E Frequencies of islets from each subcluster per donor in AA+ and T1D samples. Color indicates subcluster as in panel C.

Figure 3.F Distribution of the islets of Inflamed-I through -IV on the PAGA force-directed layout shown in Figure 2.B

Figure 3.G Differences in marker expression frequencies between CD8⁺T cells in islets from the Inflamed group and from the Insulin-Depleted + Immune group. T cells from all islets of the specified groups were pooled within each donor to compute the frequencies of marker expression. Significance was determined using the Wilcoxon signed-rank test (* $p<0.05$, ** $p<0.01$, *** $p<0.001$) and was not corrected for multiple hypothesis testing.

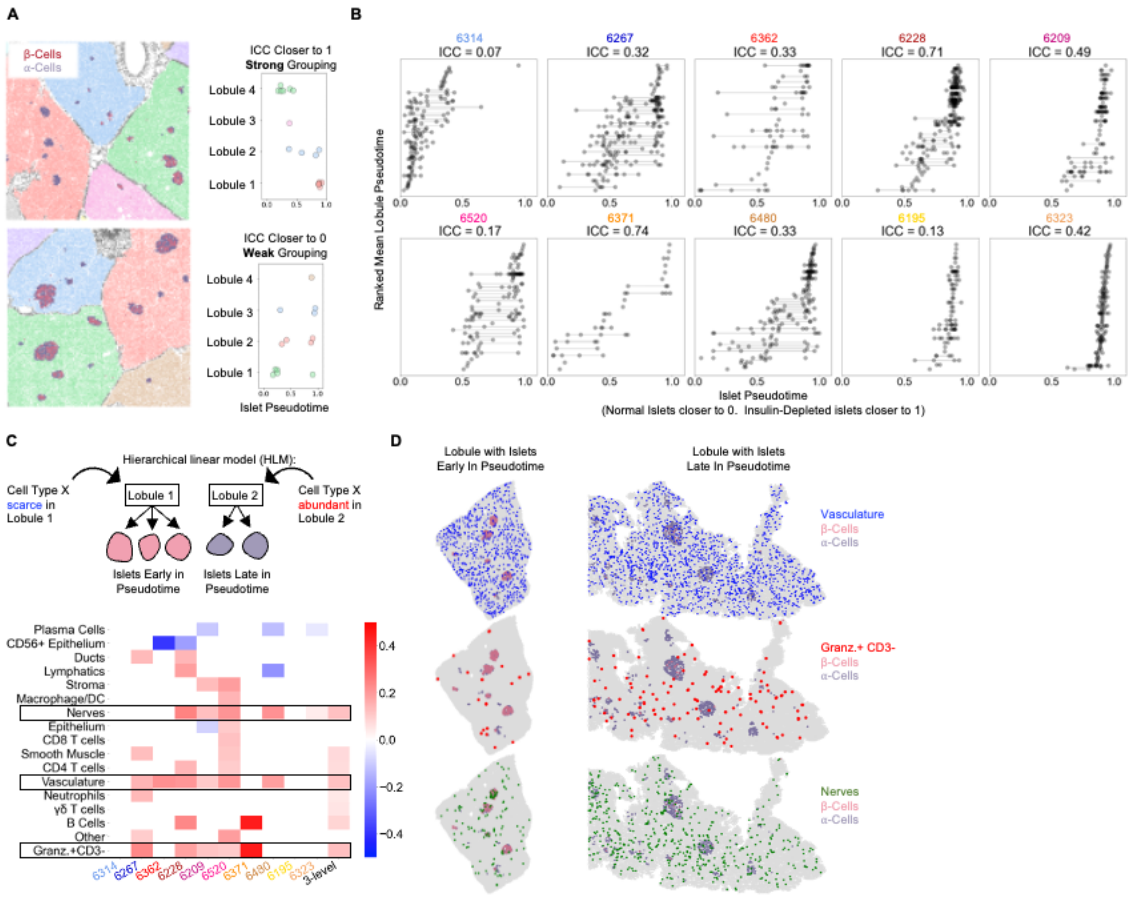

Figure 4 Vasculature, nerves, and Granzyme-B$^+$/CD3- cells in the extra-islet pancreas are associated with the lobular patterning of islet pathogenesis

Figure 4.A A schematic of the method for quantifying lobular patterning of insulitis. Lobules were segmented and colored accordingly. The islets are colored according to their composition of b-cells and a-cells. Top: A region from case 6228 with a strong lobular grouping effect and an ICC closer to 1. Bottom: A region from case 6267 with a weak lobular grouping effect and an ICC closer to 0.

Figure 4.B Lobular patterning of insulitis within each donor. Each point represents an islet. The x-axis represents the islet pseudotime. The y-axis is ordinal, representing the rank of each lobule according to the mean pseudotime of its islets. Violin plots per lobule are overlaid. Abbreviations: ICC: Intraclass correlation coefficient.

Figure 4.C Cell types associated with lobular patterning. Top: Schematic of the hierarchical linear model. Cells in islets were omitted when computing the lobular abundance of each cell-type. Bottom: Coefficients of two-level models trained on each donor separately (columns labeled by donor) and a three-level model (right column). Color corresponds to the coefficient and features with p>0.05 are white. Significance was determined using Satterthwaites's method in the lmerTest R package. No adjustment for multiple hypothesis testing was applied.

Figure 4.D Visualization of vasculature (top), Granzyme-B/CD3- cells (middle), and nerves (bottom) in two lobules. The left lobule represents lobules with islets earlier in pseudotime and a lower abundance of the given cell type in the lobule. The right lobule represents lobules with islets late in pseudotime and a greater abundance of the given cell type in the lobule.

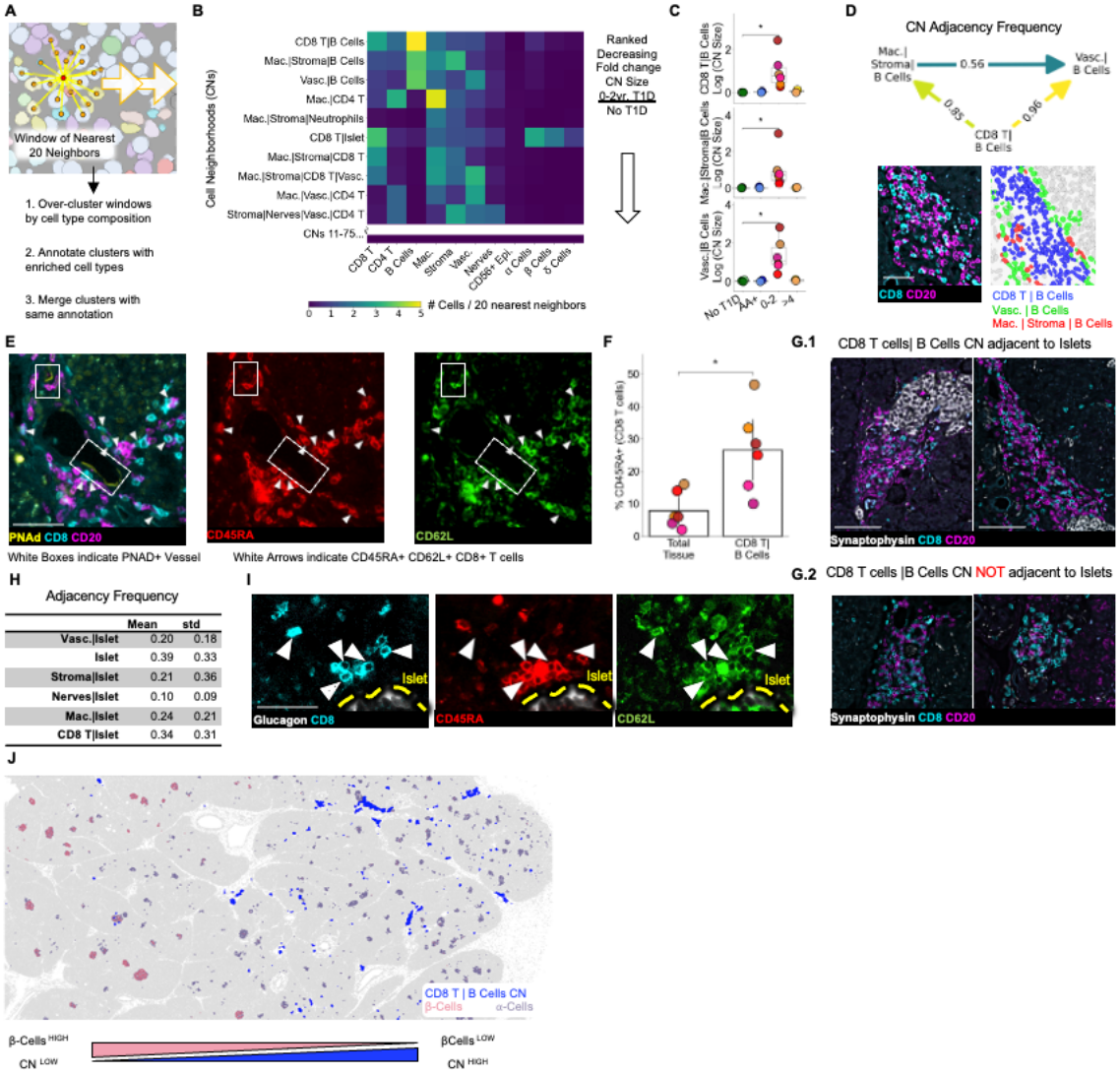

Figure 5 Immature tertiary lymphoid structures far from islets are potential staging areas for islet-destined CD8⁺T cells

Figure 5.A Schematic of algorithm for identifying CNs. Red point indicates index cell for the CN. Orange points indicate the nearest neighbors of the index cell. Windows are collected for each cell in the dataset (indicated by orange arrows).

Figure 5.B Cell-type compositions of the top CNs organized in decreasing order of the fold increase in abundance in T1D vs. non-T1D samples. Each column in the heatmap indicates the mean density of that cell type in the 20 nearest spatial neighbors of cells assigned to the CN designated for that row. CN abundance was calculated as the number of cells assigned to the given CN divided by the number of acinar cells. Abbreviations: Vasc.: vasculature; Mac.:

803 macrophage/DCs; Lym.: lymphatics. Neu.: neutrophils; CD8 T: CD8$^+$T cells; CD4 T: CD4$^+$T cells.
804 Endocrine cell types were merged during CN annotation and are labeled “Islet”.

805 Figure 5.C Mean abundances of the CD8$^+$T cell and B cell CNs per donor. Abundance was
806 calculated as the number of cells assigned to the given CN divided by the number of acinar cells.
807 Significance was determined using the Mann-Whitney U test (* $p<0.05$,** $p<0.01$, *** $p<0.001$).
808 No adjustment for multiple hypothesis testing was applied.

809 Figure 5.D Top: Adjacency frequencies of (CD8$^+$T cells| B Cell CN) with (Macrophage|Stroma|B
810 Cells) and (Vasculature| B Cells) CNs. The adjacency frequency was calculated as the number of
811 instances of the source CN adjacent to the destination CN divided by the total number of
812 instances of the source CN. Bottom Left: Raw image of a representative assembly of the three
813 CNs (CD8$^+$T cells| B Cell CN), (Macrophage|Stroma|B Cells), and (Vasculature| B Cells) displaying
814 CD8 and CD20 staining. Bottom Right: The same assembly as to the left colored by CN. Scale bar
815 indicates 50µm).

816 Figure 5.E Representative images of co-localization of PNAd$^+$ endothelium and CD45RA$^+$ CD62L$^+$
817 CD8$^+$T cells located in the (CD8$^+$T cells|B Cells) CN. Scale bar indicates 50µm.

818 Figure 5.F Frequency of CD45RA expression on CD8$^+$T cells located in (CD8$^+$T cell | B cell) CN
819 relative to CD8$^+$T cells throughout the tissue. Significance was determined with a Wilcoxon
820 signed-rank test (* $p<0.05$, ** $p<0.01$, *** $p<0.001$).

821 Figure 5.G Representative images of (CD8$^+$T cells|B Cells) instances adjacent to islets (G.1) and
822 not adjacent to islets (G.2). Scale bars indicate 200µm.

823 Figure 5.H Quantification of the adjacency frequencies between the (CD8$^+$T cells|B Cells) CN and
824 CNs rich in endocrine cells (i.e “Islet CNs”). Mean, std: mean and standard deviation adjacency
825 frequency across T1D donors. Abbreviations: Vasc.: vasculature; Mac.: macrophage.

826 Figure 5.I Representative images of islet-adjacent CD45RA$^+$ CD62L$^+$ CD8+T cells. Scale bar
827 indicates 50 µm.

828 Figure 5.J Image showing the spatial distribution of the (CD8$^+$T cells|B cells) CN instances relative
829 to islets and the enrichment of (CD8$^+$T cells|B cells) CN instances in areas of the pancreas with
830 islets lacking β-Cells.

References

Abhishek Dutta and Andrew Zisserman. 2019. "The VIA Annotation Software for Images, Audio and Video." In . MM '19. Nice, France: ACM. https://doi.org/10.1145/3343031.3350535.

Agrawal, Smriti M., Jacqueline Williamson, Ritu Sharma, Hania Kebir, Kamala Patel, Alexandre Prat, and V. Wee Yong. 2013. "Extracellular Matrix Metalloproteinase Inducer Shows Active Perivascular Cuffs in Multiple Sclerosis." *Brain* 136 (6): 1760–77. https://doi.org/10.1093/brain/awt093.

Alexander, Angela M., Megan Crawford, Suzanne Bertera, William A. Rudert, Osamu Takikawa, Paul D. Robbins, and Massimo Trucco. 2002. "Indoleamine 2,3-Dioxygenase Expression in Transplanted NOD Islets Prolongs Graft Survival After Adoptive Transfer of Diabetogenic Splenocytes:" *Diabetes* 51 (2): 356–65. https://doi.org/10.2337/diabetes.51.2.356.

Anquetil, Florence, Giada Mondanelli, Nathaly Gonzalez, Teresa Rodriguez Calvo, Jose Zapardiel Gonzalo, Lars Krogvold, Knut Dahl-Jørgensen, et al. 2018. "Loss of IDO1 Expression From Human Pancreatic β-Cells Precedes Their Destruction During the Development of Type 1 Diabetes." *Diabetes* 67 (9): 1858–66. https://doi.org/10.2337/db17-1281.

Arif, Sefina, Pia Leete, Vy Nguyen, Katherine Marks, Nurhanani Mohamed Nor, Megan Estorninho, Deborah Kronenberg-Versteeg, et al. 2014. "Blood and Islet Phenotypes Indicate Immunological Heterogeneity in Type 1 Diabetes." *Diabetes* 63 (11): 3835–45. https://doi.org/10.2337/db14-0365.

Atkinson, Mark A., and Raghavendra G. Mirmira. 2023. "The Pathogenic 'Symphony' in Type 1 Diabetes: A Disorder of the Immune System, β Cells, and Exocrine Pancreas." *Cell Metabolism* 35 (9): 1500–1518. https://doi.org/10.1016/j.cmet.2023.06.018.

Bates, Douglas, Martin Mächler, Ben Bolker, and Steve Walker. 2015. "Fitting Linear Mixed-Effects Models Using Lme4." *Journal of Statistical Software* 67 (October):1–48. https://doi.org/10.18637/jss.v067.i01.

Bender, Christine, Teresa Rodriguez-Calvo, Natalie Amirian, Ken T. Coppieters, and Matthias G. von Herrath. 2020. "The Healthy Exocrine Pancreas Contains Preproinsulin-Specific CD8 T Cells That Attack Islets in Type 1 Diabetes." *Science Advances* 6 (42): eabc5586. https://doi.org/10.1126/sciadv.abc5586.

Bhate, Salil S., Graham L. Barlow, Christian M. Schürch, and Garry P. Nolan. 2021. "Tissue Schematics Map the Specialization of Immune Tissue Motifs and Their Appropriation by Tumors." *Cell Systems*, October. https://doi.org/10.1016/j.cels.2021.09.012.

Black, Sarah, Darci Phillips, John W. Hickey, Julia Kennedy-Darling, Vishal G. Venkataraaman, Nikolay Samusik, Yury Goltsev, Christian M. Schürch, and Garry P. Nolan. 2021. "CODEX Multiplexed Tissue Imaging with DNA-Conjugated Antibodies." *Nature Protocols* 16 (8): 3802–35. https://doi.org/10.1038/s41596-021-00556-8.

Bluestone, Jeffrey A., Jane H. Buckner, and Kevan C. Herold. 2021. "Immunotherapy: Building a Bridge to a Cure for Type 1 Diabetes." *Science* 373 (6554): 510–16. https://doi.org/10.1126/science.abh1654.

Bruggeman, Brittany S., Martha Campbell-Thompson, Stephanie L. Filipp, Matthew J. Gurka, Mark A. Atkinson, Desmond A. Schatz, and Laura M. Jacobsen. 2021. "Substance Use

873 Affects Type 1 Diabetes Pancreas Pathology: Implications for Future Studies." *Frontiers*
874 *in Endocrinology* 12. https://www.frontiersin.org/articles/10.3389/fendo.2021.778912.
875 Campbell-Thompson, Martha, Ann Fu, John S. Kaddis, Clive Wasserfall, Desmond A. Schatz,
876 Alberto Pugliese, and Mark A. Atkinson. 2016. "Insulitis and β-Cell Mass in the Natural
877 History of Type 1 Diabetes." *Diabetes* 65 (3): 719–31. https://doi.org/10.2337/db15-
878 0779.
879 Campbell-Thompson, Martha, Teresa Rodriguez-Calvo, and Manuela Battaglia. 2015.
880 "Abnormalities of the Exocrine Pancreas in Type 1 Diabetes." *Current Diabetes Reports*
881 15 (10): 79. https://doi.org/10.1007/s11892-015-0653-y.
882 Campbell-Thompson, Martha, Clive Wasserfall, John Kaddis, Anastasia Albanese-O'Neill,
883 Teodora Staeva, Concepcion Nierras, Jayne Moraski, et al. 2012. "Network for
884 Pancreatic Organ Donors with Diabetes (nPOD): Developing a Tissue Biobank for Type 1
885 Diabetes." *Diabetes/Metabolism Research and Reviews* 28 (7): 608–17.
886 https://doi.org/10.1002/dmrr.2316.
887 Castro-Gutierrez, Roberto, Aimon Alkanani, Clayton E. Mathews, Aaron Michels, and Holger A.
888 Russ. 2021. "Protecting Stem Cell Derived Pancreatic Beta-Like Cells From Diabetogenic
889 T Cell Recognition." *Frontiers in Endocrinology* 12.
890 https://www.frontiersin.org/articles/10.3389/fendo.2021.707881.
891 Christoffersson, Gustaf, Sowbarnika S. Ratliff, and Matthias G. von Herrath. 2020. "Interference
892 with Pancreatic Sympathetic Signaling Halts the Onset of Diabetes in Mice." *Science*
893 *Advances* 6 (35): eabb2878. https://doi.org/10.1126/sciadv.abb2878.
894 Dalmas, Elise, Frank M. Lehmann, Erez Dror, Stephan Wueest, Constanze Thienel, Marcela
895 Borsigova, Marc Stawiski, et al. 2017. "Interleukin-33-Activated Islet-Resident Innate
896 Lymphoid Cells Promote Insulin Secretion through Myeloid Cell Retinoic Acid
897 Production." *Immunity* 47 (5): 928-942.e7.
898 https://doi.org/10.1016/j.immuni.2017.10.015.
899 Damond, Nicolas, Stefanie Engler, Vito R. T. Zanotelli, Denis Schapiro, Clive H. Wasserfall, Irina
900 Kusmartseva, Harry S. Nick, et al. 2019. "A Map of Human Type 1 Diabetes Progression
901 by Imaging Mass Cytometry." *Cell Metabolism* 29 (3): 755-768.e5.
902 https://doi.org/10.1016/j.cmet.2018.11.014.
903 Diggins, Kirsten E., Elisavet Serti, Virginia Muir, Mario Rosasco, TingTing Lu, Elisa Balmas, Gerald
904 Nepom, S. Alice Long, and Peter S. Linsley. 2021. "Exhausted-like $CD8^+$ T Cell Phenotypes
905 Linked to C-Peptide Preservation in Alefacept-Treated T1D Subjects." *JCI Insight* 6 (3).
906 https://doi.org/10.1172/jci.insight.142680.
907 Fasolino, Maria, Gregory W. Schwartz, Abhijeet R. Patil, Aanchal Mongia, Maria L. Golson, Yue J.
908 Wang, Ashleigh Morgan, et al. 2022. "Single-Cell Multi-Omics Analysis of Human
909 Pancreatic Islets Reveals Novel Cellular States in Type 1 Diabetes." *Nature Metabolism* 4
910 (2): 284–99. https://doi.org/10.1038/s42255-022-00531-x.
911 Gelman, Andrew, John B Carlin, Hal S Stern, David B Dunson, Aki Vehtari, and Donald B Rubin.
912 n.d. "Bayesian Data Analysis Third Edition (with Errors FIxed as of 15 February 2021),"
913 677.
914 Gepts, Willy. 1965. "Pathologic Anatomy of the Pancreas in Juvenile Diabetes Mellitus."
915 *Diabetes* 14 (10): 619–33. https://doi.org/10.2337/diab.14.10.619.

Goltsev, Yury, Nikolay Samusik, Julia Kennedy-Darling, Salil Bhate, Matthew Hale, Gustavo Vazquez, Sarah Black, and Garry P. Nolan. 2018. "Deep Profiling of Mouse Splenic Architecture with CODEX Multiplexed Imaging." *Cell* 174 (4): 968-981.e15. https://doi.org/10.1016/j.cell.2018.07.010.

Gregory, Gabriel A., Thomas I. G. Robinson, Sarah E. Linklater, Fei Wang, Stephen Colagiuri, Carine de Beaufort, Kim C. Donaghue, et al. 2022. "Global Incidence, Prevalence, and Mortality of Type 1 Diabetes in 2021 with Projection to 2040: A Modelling Study." *The Lancet Diabetes & Endocrinology* 10 (10): 741–60. https://doi.org/10.1016/S2213-8587(22)00218-2.

Herold, Kevan C., Brian N. Bundy, S. Alice Long, Jeffrey A. Bluestone, Linda A. DiMeglio, Matthew J. Dufort, Stephen E. Gitelman, et al. 2019. "An Anti-CD3 Antibody, Teplizumab, in Relatives at Risk for Type 1 Diabetes." *New England Journal of Medicine* 381 (7): 603–13. https://doi.org/10.1056/NEJMoa1902226.

Herold, Kevan C., Stephen E. Gitelman, Mario R. Ehlers, Peter A. Gottlieb, Carla J. Greenbaum, William Hagopian, Karen D. Boyle, et al. 2013. "Teplizumab (Anti-CD3 mAb) Treatment Preserves C-Peptide Responses in Patients With New-Onset Type 1 Diabetes in a Randomized Controlled Trial: Metabolic and Immunologic Features at Baseline Identify a Subgroup of Responders." *Diabetes* 62 (11): 3766–74. https://doi.org/10.2337/db13-0345.

Hickey, John W., Yuqi Tan, Garry P. Nolan, and Yury Goltsev. 2021. "Strategies for Accurate Cell Type Identification in CODEX Multiplexed Imaging Data." *Frontiers in Immunology* 12. https://www.frontiersin.org/article/10.3389/fimmu.2021.727626.

Hirsch, James S. 2023. "FDA Approves Teplizumab: A Milestone in Type 1 Diabetes." *The Lancet Diabetes & Endocrinology* 11 (1): 18. https://doi.org/10.1016/S2213-8587(22)00351-5.

In't Veld, Peter. 2011. "Insulitis in Human Type 1 Diabetes: The Quest for an Elusive Lesion." *Islets* 3 (4): 131–38. https://doi.org/10.4161/isl.3.4.15728.

In't Veld, Peter. 2014. "Insulitis in Human Type 1 Diabetes: A Comparison between Patients and Animal Models." *Seminars in Immunopathology* 36 (5): 569–79. https://doi.org/10.1007/s00281-014-0438-4.

Jerby-Arnon, Livnat, and Aviv Regev. 2022. "DIALOGUE Maps Multicellular Programs in Tissue from Single-Cell or Spatial Transcriptomics Data." *Nature Biotechnology* 40 (10): 1467–77. https://doi.org/10.1038/s41587-022-01288-0.

Kennedy-Darling, Julia, Salil S. Bhate, John W. Hickey, Sarah Black, Graham L. Barlow, Gustavo Vazquez, Vishal G. Venkataraaman, et al. 2021. "Highly Multiplexed Tissue Imaging Using Repeated Oligonucleotide Exchange Reaction." *European Journal of Immunology* 51 (5): 1262–77. https://doi.org/10.1002/eji.202048891.

Korpos, Éva, Nadir Kadri, Reinhild Kappelhoff, Jeannine Wegner, Christopher M. Overall, Ekkehard Weber, Dan Holmberg, Susanna Cardell, and Lydia Sorokin. 2013. "The Peri-Islet Basement Membrane, a Barrier to Infiltrating Leukocytes in Type 1 Diabetes in Mouse and Human." *Diabetes* 62 (2): 531–42. https://doi.org/10.2337/db12-0432.

Korpos, Éva, Nadir Kadri, Sophie Loismann, Clais R. Findeisen, Frank Arfuso, George W. Burke, Sarah J. Richardson, et al. 2021. "Identification and Characterisation of Tertiary Lymphoid Organs in Human Type 1 Diabetes." *Diabetologia* 64 (7): 1626–41. https://doi.org/10.1007/s00125-021-05453-z.

Krogvold, Lars, Bjørn Edwin, Trond Buanes, Johnny Ludvigsson, Olle Korsgren, Heikki Hyöty, Gun Frisk, Kristian F. Hanssen, and Knut Dahl-Jørgensen. 2014. "Pancreatic Biopsy by Minimal Tail Resection in Live Adult Patients at the Onset of Type 1 Diabetes: Experiences from the DiViD Study." *Diabetologia* 57 (4): 841–43. https://doi.org/10.1007/s00125-013-3155-y.

Kuznetsova, Alexandra, Per B. Brockhoff, and Rune H. B. Christensen. 2017. "lmerTest Package: Tests in Linear Mixed Effects Models." *Journal of Statistical Software* 82 (December):1–26. https://doi.org/10.18637/jss.v082.i13.

Lee, Michael Y., Jacob S. Bedia, Salil S. Bhate, Graham L. Barlow, Darci Phillips, Wendy J. Fantl, Garry P. Nolan, and Christian M. Schürch. 2022. "CellSeg: A Robust, Pre-Trained Nucleus Segmentation and Pixel Quantification Software for Highly Multiplexed Fluorescence Images." *BMC Bioinformatics* 23 (1): 46. https://doi.org/10.1186/s12859-022-04570-9.

Leete, Pia, Abby Willcox, Lars Krogvold, Knut Dahl-Jørgensen, Alan K. Foulis, Sarah J. Richardson, and Noel G. Morgan. 2016. "Differential Insulitic Profiles Determine the Extent of β-Cell Destruction and the Age at Onset of Type 1 Diabetes." *Diabetes* 65 (5): 1362–69. https://doi.org/10.2337/db15-1615.

Martino, Luisa, Matilde Masini, Marco Bugliani, Lorella Marselli, Mara Suleiman, Ugo Boggi, Tatiane C. Nogueira, et al. 2015. "Mast Cells Infiltrate Pancreatic Islets in Human Type 1 Diabetes." *Diabetologia* 58 (11): 2554–62. https://doi.org/10.1007/s00125-015-3734-1.

Munn, David H., and Andrew L. Mellor. 2016. "IDO in the Tumor Microenvironment: Inflammation, Counter-Regulation, and Tolerance." *Trends in Immunology* 37 (3): 193–207. https://doi.org/10.1016/j.it.2016.01.002.

Orban, Tihamer, Brian Bundy, Dorothy J. Becker, Linda A. DiMeglio, Stephen E. Gitelman, Robin Goland, Peter A. Gottlieb, et al. 2011. "Co-Stimulation Modulation with Abatacept in Patients with Recent-Onset Type 1 Diabetes: A Randomised, Double-Blind, Placebo-Controlled Trial." *Lancet (London, England)* 378 (9789): 412–19. https://doi.org/10.1016/S0140-6736(11)60886-6.

———. 2014. "Costimulation Modulation With Abatacept in Patients With Recent-Onset Type 1 Diabetes: Follow-up 1 Year After Cessation of Treatment." *Diabetes Care* 37 (4): 1069–75. https://doi.org/10.2337/dc13-0604.

Penaranda, Cristina, Qizhi Tang, Nancy H. Ruddle, and Jeffrey A. Bluestone. 2010. "Prevention of Diabetes by FTY720-Mediated Stabilization of Peri-Islet Tertiary Lymphoid Organs." *Diabetes* 59 (6): 1461–68. https://doi.org/10.2337/db09-1129.

Perdigoto, Ana Luisa, Paula Preston-Hurlburt, Pamela Clark, S. Alice Long, Peter S. Linsley, Kristina M. Harris, Steven E. Gitelman, et al. 2019. "Treatment of Type 1 Diabetes with Teplizumab: Clinical and Immunological Follow-up after 7 Years from Diagnosis." *Diabetologia* 62 (4): 655–64. https://doi.org/10.1007/s00125-018-4786-9.

Pescovitz, Mark D., Carla J. Greenbaum, Heidi Krause-Steinrauf, Dorothy J. Becker, Stephen E. Gitelman, Robin Goland, Peter A. Gottlieb, et al. 2009. "Rituximab, B-Lymphocyte Depletion, and Preservation of Beta-Cell Function." *New England Journal of Medicine* 361 (22): 2143–52. https://doi.org/10.1056/NEJMoa0904452.

Phillips, Darci, Magdalena Matusiak, Belén Rivero Gutierrez, Salil S. Bhate, Graham L. Barlow, Sizun Jiang, Janos Demeter, et al. 2021. "Immune Cell Topography Predicts Response to

PD-1 Blockade in Cutaneous T Cell Lymphoma." *Nature Communications* 12 (1): 6726. https://doi.org/10.1038/s41467-021-26974-6.

Phillips, Darci, Christian M. Schürch, Michael S. Khodadoust, Youn H. Kim, Garry P. Nolan, and Sizun Jiang. 2021. "Highly Multiplexed Phenotyping of Immunoregulatory Proteins in the Tumor Microenvironment by CODEX Tissue Imaging." *Frontiers in Immunology* 12:687673. https://doi.org/10.3389/fimmu.2021.687673.

Pugliese, Alberto, Mingder Yang, Irina Kusmarteva, Tiffany Heiple, Francesco Vendrame, Clive Wasserfall, Patrick Rowe, et al. 2014. "The Juvenile Diabetes Research Foundation Network for Pancreatic Organ Donors with Diabetes (nPOD) Program: Goals, Operational Model and Emerging Findings." *Pediatric Diabetes* 15 (1): 1–9. https://doi.org/10.1111/pedi.12097.

Richardson, Sarah J., and Alberto Pugliese. 2022. "100 YEARS OF INSULIN: Pancreas Pathology in Type 1 Diabetes: An Evolving Story." *Journal of Endocrinology* 252 (2): R41–57. https://doi.org/10.1530/JOE-21-0358.

Rodriguez-Calvo, Teresa, Olov Ekwall, Natalie Amirian, Jose Zapardiel-Gonzalo, and Matthias G. von Herrath. 2014. "Increased Immune Cell Infiltration of the Exocrine Pancreas: A Possible Contribution to the Pathogenesis of Type 1 Diabetes." *Diabetes* 63 (11): 3880–90. https://doi.org/10.2337/db14-0549.

Rovituso, Damiano M., Laura Scheffler, Marie Wunsch, Christoph Kleinschnitz, Sebastian Dörck, Jochen Ulzheimer, Antonios Bayas, Lawrence Steinman, Süleyman Ergün, and Stefanie Kuerten. 2016. "CEACAM1 Mediates B Cell Aggregation in Central Nervous System Autoimmunity." *Scientific Reports* 6 (July):29847. https://doi.org/10.1038/srep29847.

Saelens, Wouter, Robrecht Cannoodt, Helena Todorov, and Yvan Saeys. 2019. "A Comparison of Single-Cell Trajectory Inference Methods." *Nature Biotechnology* 37 (5): 547–54. https://doi.org/10.1038/s41587-019-0071-9.

Sainburg, Tim, Leland McInnes, and Timothy Q. Gentner. 2021. "Parametric UMAP Embeddings for Representation and Semi-Supervised Learning." arXiv. https://doi.org/10.48550/arXiv.2009.12981.

Sarkar, Suparna A., Randall Wong, Seija I. Hackl, Ong Moua, Ronald G. Gill, Alexander Wiseman, Howard W. Davidson, and John C. Hutton. 2007. "Induction of Indoleamine 2,3-Dioxygenase by Interferon-Gamma in Human Islets." *Diabetes* 56 (1): 72–79. https://doi.org/10.2337/db06-0617.

Savinov, Alexei Y., F. Susan Wong, Austin C. Stonebraker, and Alexander V. Chervonsky. 2003. "Presentation of Antigen by Endothelial Cells and Chemoattraction Are Required for Homing of Insulin-Specific CD8+ T Cells." *The Journal of Experimental Medicine* 197 (5): 643–56. https://doi.org/10.1084/jem.20021378.

Schürch, Christian M., Salil S. Bhate, Graham L. Barlow, Darci J. Phillips, Luca Noti, Inti Zlobec, Pauline Chu, et al. 2020. "Coordinated Cellular Neighborhoods Orchestrate Antitumoral Immunity at the Colorectal Cancer Invasive Front." *Cell*, August. https://doi.org/10.1016/j.cell.2020.07.005.

Shekarian, Tala, Carl P. Zinner, Ewelina M. Bartoszek, Wandrille Duchemin, Anna T. Wachnowicz, Sabrina Hogan, Manina M. Etter, et al. 2022. "Immunotherapy of Glioblastoma Explants Induces Interferon-γ Responses and Spatial Immune Cell

Rearrangements in Tumor Center, but Not Periphery." bioRxiv. https://doi.org/10.1101/2022.01.19.474897.

Wang, Yue J., Daniel Traum, Jonathan Schug, Long Gao, Chengyang Liu, Mark A. Atkinson, Alvin C. Powers, et al. 2019. "Multiplexed In Situ Imaging Mass Cytometry Analysis of the Human Endocrine Pancreas and Immune System in Type 1 Diabetes." *Cell Metabolism* 29 (3): 769-783.e4. https://doi.org/10.1016/j.cmet.2019.01.003.

Wekerle, Hartmut. 2017. "B Cells in Multiple Sclerosis." *Autoimmunity* 50 (1): 57–60. https://doi.org/10.1080/08916934.2017.1281914.

Wilcox, Nicholas S, Jinxiu Rui, Matthias Hebrok, and Kevan C Herold. 2016. "Life and Death of β Cells in Type 1 Diabetes: A Comprehensive Review." *Journal of Autoimmunity* 71 (July):51–58. https://doi.org/10.1016/j.jaut.2016.02.001.

Wolf, F. Alexander, Fiona K. Hamey, Mireya Plass, Jordi Solana, Joakim S. Dahlin, Berthold Göttgens, Nikolaus Rajewsky, Lukas Simon, and Fabian J. Theis. 2019. "PAGA: Graph Abstraction Reconciles Clustering with Trajectory Inference through a Topology Preserving Map of Single Cells." *Genome Biology* 20 (1): 59. https://doi.org/10.1186/s13059-019-1663-x.

Yi, Nengjun, Zaixiang Tang, Xinyan Zhang, and Boyi Guo. 2019. "BhGLM: Bayesian Hierarchical GLMs and Survival Models, with Applications to Genomics and Epidemiology." *Bioinformatics* 35 (8): 1419–21. https://doi.org/10.1093/bioinformatics/bty803.

Yoshihara, Eiji, Carolyn O'Connor, Emanuel Gasser, Zong Wei, Tae Gyu Oh, Tiffany W. Tseng, Dan Wang, et al. 2020. "Immune-Evasive Human Islet-like Organoids Ameliorate Diabetes." *Nature* 586 (7830): 606–11. https://doi.org/10.1038/s41586-020-2631-z.

Ziegler, Anette G., Marian Rewers, Olli Simell, Tuula Simell, Johanna Lempainen, Andrea Steck, Christiane Winkler, et al. 2013. "Seroconversion to Multiple Islet Autoantibodies and Risk of Progression to Diabetes in Children." *JAMA* 309 (23): 2473–79. https://doi.org/10.1001/jama.2013.6285.

Acknowledgements

This research was performed with the support of the Network for Pancreatic Organ donors with Diabetes (nPOD; RRID:SCR_014641), a collaborative type 1 diabetes research project supported by JDRF (nPOD: 5-SRA-2018-557-Q-R) and The Leona M. & Harry B. Helmsley Charitable Trust (Grant#2018PG-T1D053, G-2108-04793). The content and views expressed are the responsibility of the authors and do not necessarily reflect the official view of nPOD. Organ Procurement Organizations (OPO) partnering with nPOD to provide research resources are listed at http://www.jdrfnpod.org/for-partners/npod-partners/. Research reported in this publication was supported by the National Cancer Institute and National Institute of Allergy and Infectious Diseases of the National Institutes of Health under Award Numbers K99CA246061, 5U54CA209971-05, 5U2CCA233195-02, 1U2CCA233238-01, 5U2CCA233195-02, 5U01AI101984-09. The content is solely the responsibility of the authors and does not necessarily represent the official views of the National Institutes of Health. C.M.S. was supported by the Swiss National Science Foundation (P300PB_171189, P400PM_183915). We like to thank Yury Goltsev, Pauline Chu, Sarah Black, Gustavo Vazquez, Aviv Hargil (Stanford University), and Irina Kusmartseva (nPOD) for excellent assistance. We like to thank Dr. Xavier Rovira-Clavé (Stanford University) for critical comments on the manuscript.

Author information

G.L.B curated data, wrote software, and analyzed data. D.P. and C.M.S contributed significantly to validating the antibody panel and assisted with analysis. S.D., S.S.B, A.Y., H.A.M., G.K.K., N.N., S.R., and J.M. assisted with analysis. G.L.B., J.A.B., G.P.N., and P.L.B., conceptualized the study and wrote the manuscript. All authors have read and approved the final version of the manuscript.

Ethics declarations

P.L.B.: Founder, Halo Biosciences.

N.N.: Founder, Halo Biosciences.

PLB, NN and GK have filed intellectual property around 4-MU. PLB, NN and GK hold a financial interest in Halo Biosciences, a company that is developing 4-MU for various indications.

G.P.N. has received research grants from Vaxart and Celgene during the course of this work and has equity in and is a scientific advisory board member of Akoya Biosciences. Akoya Biosciences makes reagents and instruments that are dependent on licenses from Stanford University. Stanford University has been granted US patent 9909167, which covers some aspects of the technology described in this paper.

J.A.B.: Board of director for Gilead and CEO and President of Sonoma Biotherapeutics; scientific advisory boards of Arcus Biotherapeutics and Cimeio Therapeutics; consultant for Rheos Medicines, Provention Bio; stockholder in Rheos Medicines, Vir Therapeutics, Arcus Biotherapeutics, Solid Biosciences, Celsius Therapeutics; Gilead Sciences, Provention Bio, Sonoma Biotherapeutics.

C.M.S.: Scientific advisory board of, stock options in, research funding from Enable Medicine, Inc.

Supplemental Information

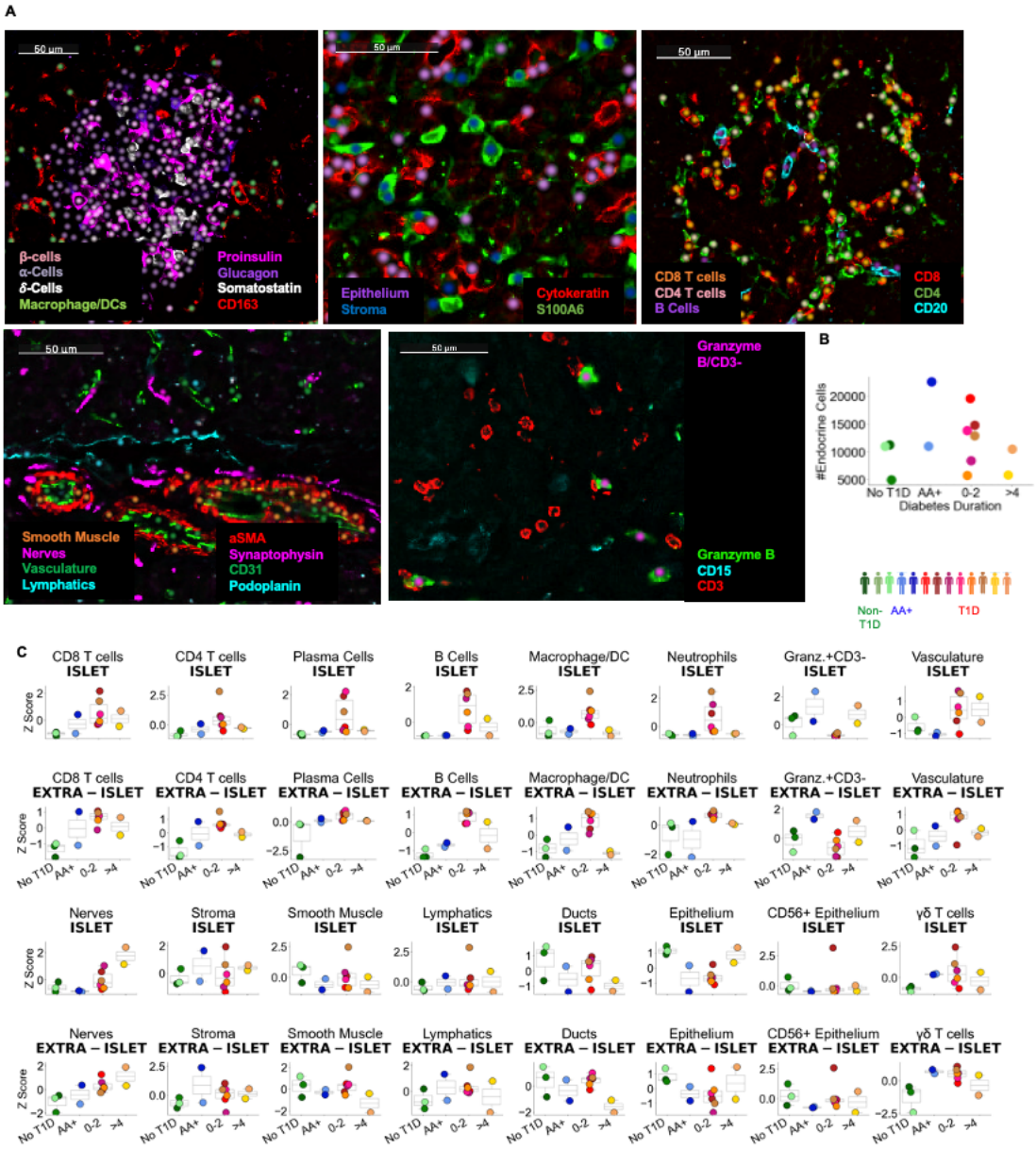

Supplemental Figure 1 Related to Figure 1.

Supplemental Figure 1.A Validation of cell annotations. Dots were overlaid on images of characteristic markers colored by cell type. In each panel, the cell types and their corresponding colors are indicated and the markers and their corresponding colors are specified.

Supplemental Figure 1.B The total number of endocrine cells measured in each donor.

Supplemental Figure 1.C Changes in cellular abundance in Islet (top) and extra-islet (bottom) regions. The Y-axis corresponds to the number of the given cell type / number of endocrine cells in the top row and the number of a given cell type / number of acinar cells in the bottom row in each donor. These frequencies were then z-normalized across donors.

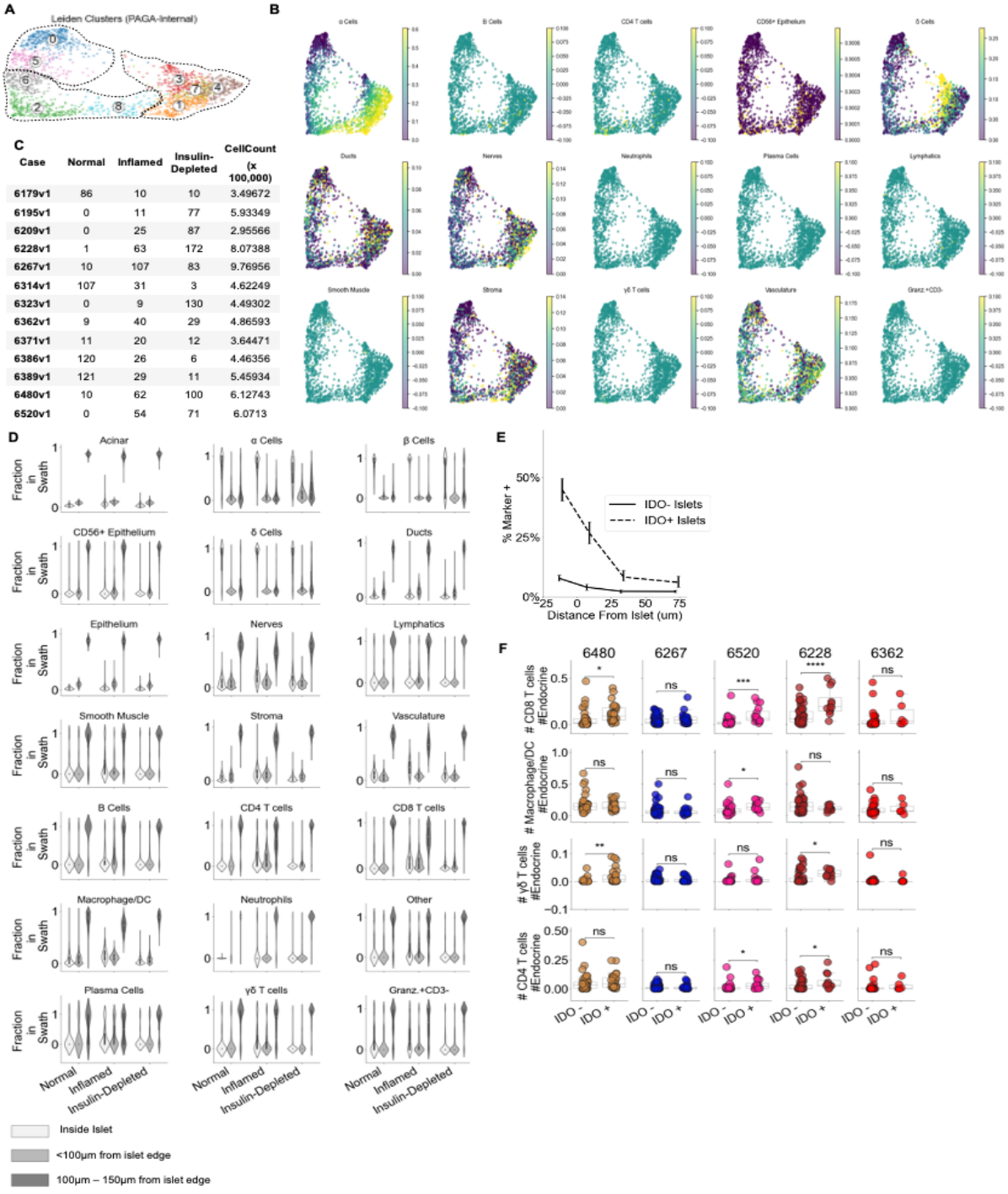

Supplemental Figure 2 Related to Figure 2.

Supplemental Figure 2.A Leiden clustering computed by PAGA algorithm internally. Clusters 0 and 5 were assigned to the 'Healthy' group. Clusters 6, 2, and 8 were assigned to the "Inflamed" group. Clusters 1,3,7, and 4 were assigned to the "Insulin-Depleted" group.

Supplemental Figure 2.B The density of other cell types per islet across pseudotime. Same as Figure 2.E.

Supplemental Figure 2.C The number of islets of each stage of pseudotime and the total number of cells per case.

Supplemental Figure 2.D For each cell type, the frequency of that cell type inside islets, within 100µm of the islet edge, and 100µm-150µm from the islet edge was quantified.

Supplemental Figure 2.E Frequency of IDO on vasculature at different distances from islets. Dashed line indicates the frequency in and around islets where IDO^+ was detected in islet vasculature (n=84) as in Figure 2.H. Solid line indicates the frequency in and around Inflamed Islets in which IDO was absent in islet vasculature (n=267). Error bars indicate 95% confidence intervals obtained by iteratively calculating the marker frequency in re-sampled islets with replacement (n=200)

Supplemental Figure 2.F $CD8^+$T cell, Macrophage, γ/δ T cell, and $CD4^+$T cell abundance in IDO^+ and IDO^- islets. Same as Figure 2.I. Asterisks in figure indicate significance within each donor (Satterthwaites's method lmerTest R package).

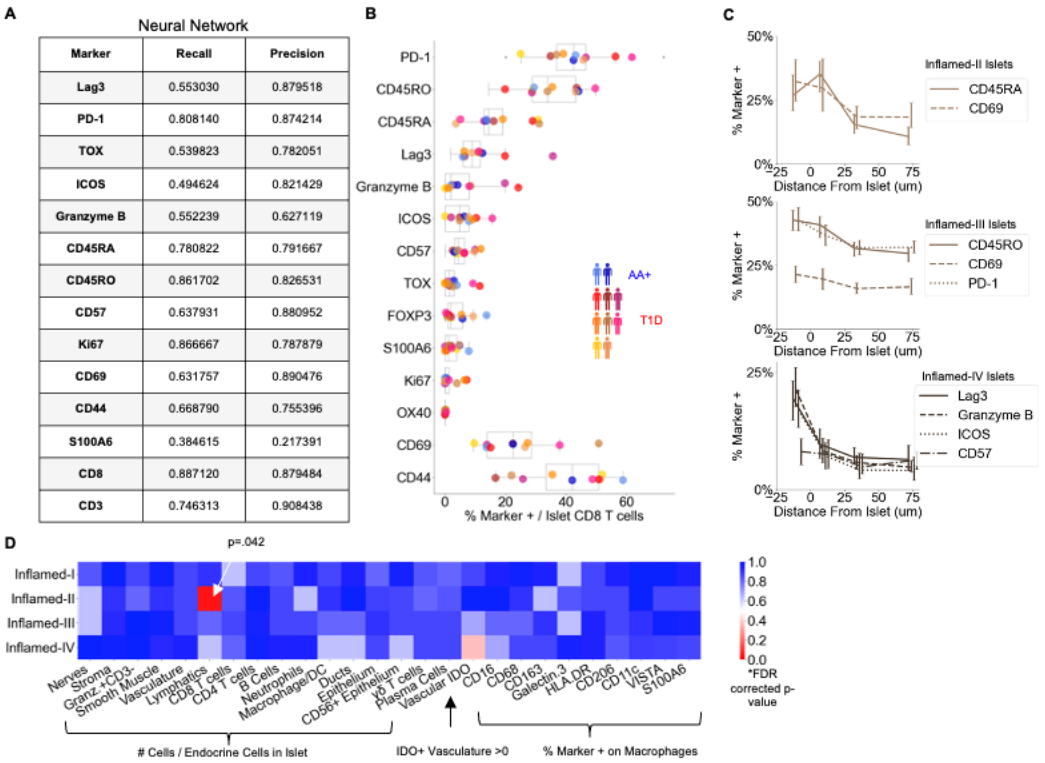

Marker	Recall	Precision
Lag3	0.553030	0.879518
PD-1	0.808140	0.874214
TOX	0.539823	0.782051
ICOS	0.494624	0.821429
Granzyme B	0.552239	0.627119
CD45RA	0.780822	0.791667
CD45RO	0.861702	0.826531
CD57	0.637931	0.880952
Ki67	0.866667	0.787879
CD69	0.631757	0.890476
CD44	0.668790	0.755396
S100A6	0.384615	0.217391
CD8	0.887120	0.879484
CD3	0.746313	0.908438

Supplemental Figure 3 Related to Figure 3

Supplemental Figure 3.A Validation of neural network for detecting expression of T cell markers. Recall and Precision for the neural network. The table was computed using cells in the "Test" dataset.

Supplemental Figure 3.B Frequency of functional markers on $CD8^{+}$T cells inside islets. Colors correspond to donor. Only AA+ and T1D donors are displayed.

Supplemental Figure 3.C Frequency of functional markers on $CD8^{+}$T cells at different distances from islets. Error bars indicate 95% confidence intervals obtained by iteratively calculating the marker frequency in re-sampled islets with replacement (n=200).

Supplemental Figure 3.D Association of islet features with Inflamed-I through -IV. For each feature (columns), a mixed-level model adjusting for donor was fit in a one-vs-all design and the p-value was determined using Satterthwaites's method in lmerTest R package. Values in the heatmap were corrected for multiple hypotheses using the Benjamini, Hochberg method.

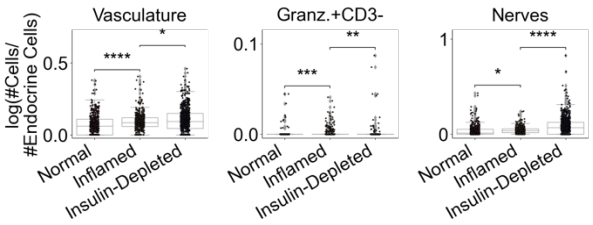

Supplemental Figure 4 Related to Figure 4

Supplemental Figure 4 Changes in cell types identified by HLM in insulitis. Each point represents and islet. Islets are grouped according to the pseudotime analysis from Figure 2. The y-axis corresponds to the log-transformed values for the number of the given cell type / number of endocrine cells. Significance was determined using the t-test (* p<0.05,** p<0.01, *** p<0.001). No adjustment for multiple hypothesis testing was applied.

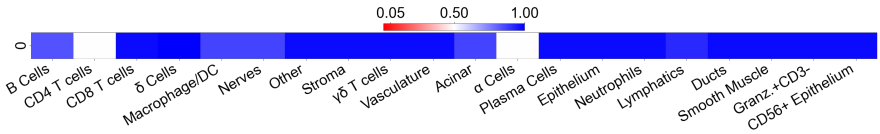

Supplemental Figure 5 Related to Figure 5

Supplemental Figure 5 Association of the cell composition of the $CD8^{+}$T cells|B Cells CN with islet proximity. For each feature (columns), a mixed-level model adjusting for donor was fit against instances that were or were not < 20µm from an islet and the p-value was determined using Satterthwaites's method in lmerTest R package. Values in the heatmap were corrected for multiple hypotheses using the Benjamini, Hochberg method.

CaseID	Donor Type	Age (years)	Diabetes Duration (years)	Cause of Death	Sex	Ethnicity	BMI	nPOD RRID
6267	Autoab positive	23	NA	Anoxia	Female	Caucasian	16.59	SAMN15879321
6314	Autoab positive	21	NA	Head Trauma	Male	Caucasian	23.8	SAMN15879368
6520	T1D	21.61	0	Cerebrovascular/	Male	Caucasian	29.3	SAMN18053203
6362	T1D	24.9	0	Head Trauma	Male	Caucasian	28.5	SAMN15879415
6228	T1D	13	0	Anoxia	Male	Caucasian	17.4	SAMN15879284
6209	T1D	5	0.25	Cerebral edema secondary to DKA	Female	Caucasian	15.9	SAMN15879265
6371	T1D	12.5	2	Cerebral edema	Female	Caucasian	16.6	SAMN15879424
6480	T1D	17.18	2	DKA	Male	Caucasian	27.1	SAMN15879533
6195	T1D	19.3	5	Head Trauma	Male	Caucasian	23.7	SAMN15879251
6323	T1D	22	6	Anoxia	Female	Caucasian	24.7	SAMN15879377
6389	No diabetes	18.6	NA	Head Trauma	Male	Caucasian	20.9	SAMN15879442
6179	No diabetes	20	NA	Head Trauma	Female	Caucasian	20.7	SAMN15879235
6386	No diabetes	14	NA	Head Trauma	Male	Caucasian	23.9	SAMN15879439

Supplemental Table 1: **nPOD Case Information**

Both	"All" UMAP	"Immune" UMAP	Endocrine Cells	Un-used ****
Channel 2 Blank*	alphaSMA	VISTA	Glucagon	CD44
Channel 3 Blank*	Synaptophysin	TCR g/d	Insulin	CD45RA
Channel 4 Blank*	Podoplanin	MPO	Proinsulin	CD45RO
S100A6	PD-L1 ***	HLA-DR	Somatostatin	CollIV
Hoechst**	NaKATPase	FOXP3		HABP
Granzyme B	MUC-1	CD8		HLA-ABC
Galectin-3	Draq 5	CD69		ICOS
CD68	Cytokeratin	CD4		IDO
CD57	Chromogranin A	CD206		Ki67
CD56	CD31	CD16		Lag3
CD45		CD11c		OX40
CD3		BCL-2		PD-1
CD20				TOX
CD163				
CD15				
CD138				

Supplemental Table 2: **Markers used for cell-type identification.** Channels in the "Both" column were used for clustering all cells and specifying immune cells. Channels in the "All" column were only used for clustering all cells and the UMAP in Figure 1.B. Channels in "Immune" columns were only used for sub-clustering immune cells and the UMAP in Figure 1.C. Channels in "Endocrine" column were used for sub-clustering endocrine populations. Channels in "Un-used" column were not included in the clustering or UMAP step because they were either too weak to aid clustering or were expressed on multiple cell-populations and confounded cell-type identification.

Main Panel

	AntiBody	A488	ExposuresTime	AntiBody	A555	ExposuresTime	AntiBody	A647	ExposuresTime
Cycle 1	CollIV	33	333	NaKATPase	36	100	HLA-ABC	53	100
Cycle 2	blank	blank	1000	blank	blank	1000	blank	blank	1000
Cycle 3	Ki67	6	100	BCL-2	46	500	TOX	28	150
Cycle 4	Chromogranin A	43	16	empty		1	FOXP3	61	1000
Cycle 5	Proinsulin	63	40	Galectin-3	60	166	empty		1
Cycle 6	Glucagon	24	50	Podoplanin	32	500	Insulin	30	200
Cycle 7	CD8	8	125	CD31	68	100	Lag3	42	500
Cycle 8	CD15	14	40	CD45RA	7	333	PD-1	23	500
Cycle 9	MPO	51	117	CD69	52	500	PD-L1	11	500
Cycle 10	S100A6	70	500	empty		1	CD3	77	500
Cycle 11	MUC-1	21	33	CD20	48	167	CD4	20	500
Cycle 12	Cytokeratin	67	100	CD16	15	250	CD11c	49	500
Cycle 13	alphaSma	69	50	CD163	45	100	empty		1
Cycle 14	CD57	57	300	Somatostatin	2	100	CD56	29	333
Cycle 15	CD44	44	250	CD206	55	400	CD45RO	3	500
Cycle 16	TCR g/d	72	1000	CD45	56	250	ICOS	41	500
Cycle 17	empty		1	Synaptophysin	26	250	Granzyme B	81	100
Cycle 18	empty		1	HLA-DR	65	250	OX40	66	400
Cycle 19	empty		1	VISTA	79	500	CD138	76	200
Cycle 20	empty		1	IDO	59	2500	CD68	5	100
Cycle 21	empty		1	HABP	1/100 StrPE	13	Draq 5		115

Tertiary Lymphoid Structure Panel

	AntiBody	A488	ExposuresTime	AntiBody	A555	ExposuresTime	AntiBody	A647	Dilution
Cycle 1	Chromogranin A	43	16	CD20	48	167	CD3	77	500
Cycle 2	Proinsulin	63	40	CD31	68	100	CD45RO	3	500
Cycle 3	CD8	8	125	CD45RA	7	333	CD4	20	500
Cycle 4	Ki67	6	100	Podoplanin	32	500	CD138	76	200
Cycle 5	Glucagon	24	50	CD62L	38	250	PnAD	71	333
Cycle 6	alphaSma	69	50				ColIIV	33	333

Supplemental Table 3: CODEX Experiment Details

Marker	Clone	Vendor	Identifier
ColIIV	poly	Abcam	ab6586
Ki67	B56	BD	556003
Chromogranin A	.K2H10 + PHE5 + CGA/41	Novus	NBP2-34674
Proinsulin	3A1	Thermo	MA122710
Glucagon	K7bB10	Abcam	ab10988
CD8	C8/144B	Santa Cruz	sc-53212
CD15	MMA	BD	559045
MPO	poly	R&D	AF3667
S100A6	7D11	Novus	NB100-1765
MUC-1	955	NSJ Bioreagents	V2372SAF
Cytokeratin	C11	Biolegend	628602
alphaSma	polyclonal	abcam	ab5694
CD57	HCD57	Biolegend	359602
CD44	IM-7	Biolegend	103002
TCR g/d	H-41	Santa Cruz	sc-100289
NaKATPase	EP1845Y	Abcam	ab167390
BCL-2	124	Cell Marque	custom
Galectin-3	A3A12	Thermo	MA1940
Podoplanin	NC-08	Biolegend	916606
CD31	C31.3 + C31.7 + C31.10	Novus Bio	NBP2-47785
CD45RA	HI100	Biolegend	555486
CD69	poly (AF2359)	Novus	AF2359
CD20	rIGEL/773	Novus	NBP2-54591
CD16	D1N9L	CST	custom
CD163	EDHu-1	Novus	NB110-40686
Somatostatin	7G5	Novus	NBP2-37447
CD206	poly	R&D	AF2534
CD45	2B11 + PD7/26	Novus	NBP2-34528
Synaptophysin	7H12	Novus	NBP1-47483
HLA-DR	EPR3692	abcam	ab215985
VISTA	D1L2G	CST	custom
IDO	D5J4E	CST	custom
biotinylated Hyaluronan Binding Protein (HABP)	Bollyky Lab Stanford University		custom
HLA-ABC	EMR8-5	BD	565292
TOX	E6I3Q	CST	custom
FOXP3	236A/E7	Invitrogen	14-4777-80
Insulin	K36AC10	Sigma	SAB4200691
Lag3	D2G4O	CST	custom
PD-1	D4W2J	CST	custom
PD-L1	E1L3N	CST	custom
CD3	D7A6E	CST	custom
CD4	EPR6855	Abcam	ab181724
CD11c	EP1347Y	AbCam	ab216655
CD56	MRQ-42	Cell Marque	custom
CD45RO	UCH-L1	Santa Cruz	sc-1183
ICOS	D1K2T	CST	custom
Granzyme B	EPR20129-217	Abcam	ab219803
OX40	Ber-ACT35	Biolegend	Ber-ACT35
CD138	B-A38	Invitrogen	MA1-10091
CD68	D4B9C	CST	916104
PNAD	MECA-79	Biolegend	120801
CD62L	B-8	SCBT	QT 48070

Supplemental Table 4: Antibody Clone Details